Experimental Studies of Dzyaloshinskii-Moriya Interaction in Quantum Spin Systems: High-frequency High-field Electron Spin Resonance (ESR) Measurements

Ohta, Hitoshi

(Citation)
Journal of the Physical Society of Japan,92(8):081003

(Issue Date)
2023-08-15

(Resource Type)
journal article

(Version)
Version of Record

(URL)
https://hdl.handle.net/20.500.14094/0100482174

Journal of the Physical Society of Japan **92**, 081003 (2023)
https://doi.org/10.7566/JPSJ.92.081003

Experimental Studies of Dzyaloshinskii–Moriya Interaction in Quantum Spin Systems: High-frequency High-field Electron Spin Resonance (ESR) Measurements

Hitoshi Ohta*

Molecular Photoscience Research Center, Kobe University, Kobe 657-8501, Japan

(Received November 1, 2022; accepted February 9, 2023; published online May 9, 2023)

In this review, the importance of the Dzyaloshinskii–Moriya Interaction (DMI) to the magnetic properties of quantum spin systems is discussed mainly focusing on the determination of or understanding the role of DMI extracted from high-frequency high-field electron spin resonance (ESR) measurements. This review includes the ESR theories of the $S = 1/2$ one-dimensional (1D) antiferromagnet with the staggered field (Oshikawa–Affleck theory) and with the uniform DMI, and several related experimental results are shown. Then, the proposed mechanisms of the singlet–triplet transition in quantum spin systems together with the ESR selection rules are introduced in connection with various experimental results. Finally, the role of DMI in the ground state of kagome lattice antiferromagnets and the honeycomb lattice antiferromagnet is discussed with some experimental results.

1. Introduction

The Dzyaloshinskii–Moriya interaction (DMI) was suggested by Dzyaloshinskii[1] from purely symmetry grounds, and Moriya[2] developed a theory by extending the Anderson theory of superexchange to include spin–orbit coupling through the second-order perturbation. The DMI term is expressed by

$$\mathbf{D} \cdot (\boldsymbol{S}_i \times \boldsymbol{S}_j), \tag{1}$$

where a modern textbook[3] says that "The form of the interaction is such that it tries to force $\boldsymbol{S}_i$ and $\boldsymbol{S}_j$ to be at right angles in a plane perpendicular to the vector $\mathbf{D}$ in such an orientation as to ensure that the energy is negative". The vector $\mathbf{D}$ will not vanish in general, whereas it vanishes when the crystal field has an inversion symmetry between the two magnetic ions. Moriya also discussed how the symmetry between the two magnetic ions will restrict the direction of $\mathbf{D}$.[2] As discussed by Moriya,[2] the orders of the magnitude of $\mathbf{D}$ can be estimated by

$$D \sim (\Delta g/g)J, \tag{2}$$

where g, Δg, and J are the g-value, its deviation from the value for a free electron, and the exchange interaction between the two magnetic ions, respectively. This is because both D and Δg are related to the second-order perturbation of the spin–orbit coupling. In particular, as the form of Δg is related to that of Pryce spin Hamiltonian, Δg obtained from the electron spin resonance (ESR) is suitable. DMI [Eq. (1)] tends to cant the spins by a small angle, which induces a small ferromagnetic component of the moments in antiferromagnets such as α-Fe_2O_3, $MnCO_3$, and $CoCO_3$. This effect is known as a weak ferromagnetism, whose overall magnetic properties can be interpreted on the basis of the mean-field theory by including a small DMI term (1) in the case of three-dimensional antiferromagnets.

However, recently, it has become clear that DMI plays important roles in many aspects of quantum spin systems and the ESR observations in them. The $S = 1/2$ one-dimensional (1D) Heisenberg antiferromagnet is known as a typical quantum spin system that will not show the Néel order even at 0 K and is beyond the scope of the mean-field theory. The Oshikawa–Affleck developed an ESR theory of $S = 1/2$ quantum spin chain with the staggered field, which can also be induced by DMI, using the field-theory approach.[4–6] Oshikawa and Affleck theory was able to interpret the unsolved ESR behavior in Cu benzoate[7] by assuming DMI, and more extended ESR experiments related to the theory will be discussed in Sect. 2.1. On the other hand, if one considers the ESR of the $S = 1/2$ antiferromagnetic chain with the uniform DMI, the splitting of the ESR mode is expected theoretically owing to the momentum shift of the spinon spectrum by DMI and actually observed for $\mathbf{H} \parallel \mathbf{D}$,[8] which will be discussed in Sect. 2.2. Recent experimental extensions to the high frequency and high magnetic field for ESR[9,10] revealed many direct transitions between the singlet and triplet states in quantum spin system, which should be forbidden for the conventional magnetic dipole transition. These ESR experimental examples and the mechanisms related to DMI or the selection rules will be discussed in Sect. 2.3. Strong frustrations in antiferromagnetic systems will prevent the Néel order, and small perturbations such as DMI will play an important role in determining the ground state. Therefore, the role of DMI and its experimental determination in kagome antiferromagnets will be discussed in Sects. 3.1 and 3.2. Finally, the role of DMI and its experimental determination in a honeycomb lattice antiferromagnet with the frustration due to the next-nearest-neighbor antiferromagnetic exchange interaction will be discussed in Sect. 3.3.

2. ESR and DMI

2.1 *Oshikawa–Affleck (OA) theory: ESR theory for $S = 1/2$ 1D antiferromagnet with staggered field*

A theory of ESR in the $S = 1/2$ 1D antiferromagnet (J: exchange interaction) with the staggered field is developed using the field theory method by Oshikawa and Affleck.[4–6] In compounds with a low crystal symmetry, the effective staggered field ($h = cH$ where c is a constant) will be induced by the staggered g-tensor or DMI under the uniform applied field H. The considered Hamiltonian is

$$\mathcal{H} = J \sum \boldsymbol{S}_i \cdot \boldsymbol{S}_{i+1} + h \sum_i (-1)^i S_i^x - H \sum_i S_i^z, \tag{3}$$

where the first term is the isotropic Heisenberg exchange interaction for the 1D antiferromagnet, the second term is the transverse staggered field, and the third term is the Zeeman term. In real materials, the second term mainly originates from the staggered local crystal field around the magnetic ions. Therefore, the separation between the staggered g-tensor and DMI becomes relatively difficult in the analyses of the experiments.

Main conclusions by Oshikawa and Affleck can be summarized briefly as follows depending on the temperature (T) regions.

i) In the extreme low-T limit ($T \ll E_g$, breather regime), the first-breather mode

$$h\nu = \sqrt{(g\mu_B H)^2 + E_g(H)^2} \tag{4}$$

will be observed by ESR based on the sine-Gordon model,[11] where h, ν, g, μ_B, and $E_g(H) \propto H^{2/3}$ are Planck's constant, ESR frequency, g-value, Bohr magneton, and excitation gap or field-induced gap, respectively.

ii) In the temperature range E_g, $H \ll T \ll J$ (spinon regime), the following shift $\delta\omega$ and width δH of ESR are suggested

$$\delta\omega \propto (H/T)^3, \tag{5}$$

$$\delta H \propto (H/T)^2. \tag{6}$$

iii) As another contribution to the width in the temperature region $T \ll J$, a linear T-dependence of the width,

$$\delta H \propto T, \tag{7}$$

is obtained when OA field theory approach was applied to the exchange anisotropy.

Oshikawa and Affleck compared their theoretical results with the previous ESR experimental data[7,12] on Cu benzoate [$Cu(C_6H_5COO)_2{\cdot}3H_2O$] assuming the DM vector $(D_{a''}, D_{c''}) = (0.13, 0.02)J$, where $J = 8.6\,\mathrm{K}$.[4] Although originally the increase in linewidth with decreasing T shown in Fig. 1 was interpreted as the line broadening approaching the Néel order,[7] there is no evidence of Néel order from neutron scattering and susceptibility measurements.[13] On the other hand, Eq. (6) can be used to interpret the temperature and frequency dependences of the linewidth very well as shown in Fig. 1 in the frequency region from 9.4 to 48.9 GHz. Here, because the resonance field H is proportional to the frequency from the resonance condition of ESR, the frequency dependence corresponds to the H dependence in Eqs. (5) and (6). Moreover, the lowest breather excitation from Eq. (4) can be used to interpret the angular dependence at 0.41 K as shown in Fig. 2. Therefore, the OA theory seems to be consistent with the ESR experimental results of Cu benzoate up to 48.9 GHz.

To confirm the OA theory, particularly the existence of the breather, the ESR measurement of Cu benzoate was performed in a much wider frequency region up to values above 600 GHz by Asano et al.[14] The temperature dependence of linewidth shown in Fig. 3(a) clearly shows the crossover from the spinon ESR line (closed circles) to the breather ESR line (closed triangles). The leading term of the fitting function [solid line in Fig. 3(a)] is $\alpha(H/T)^2$ ($\alpha = 0.087\ [\mathrm{K^2\,T^{-1}}]$) with a small contribution of βH ($\beta = 0.007$, dimensionless). Although the origin of the βH term is unclear, the functional form predicted by the OA theory [Eq. (6)] for the spinon regime is applicable because the term

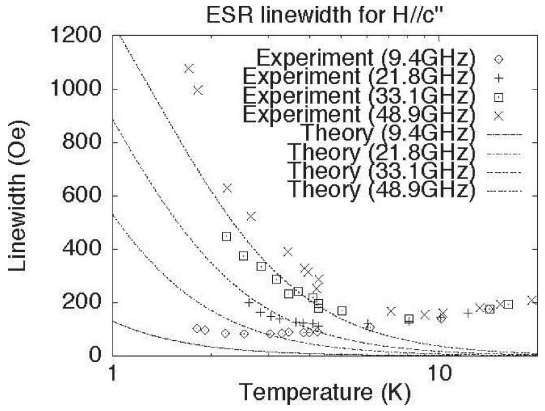

Fig. 1. Temperature and frequency dependences of ESR linewidth for $H \,//\, c''$ of Cu benzoate [$Cu(C_6H_5COO)_2{\cdot}3H_2O$],[7] compared to Eq. (6). This figure is taken from Ref. 4. © (1999) American Physical Society.

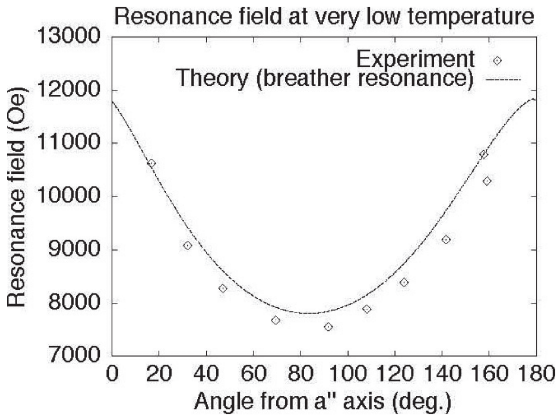

Fig. 2. Resonance field at very low temperature for various field directions in the ac plane of Cu benzoate. The experimental data were taken from the "antiferromagnetic resonance" in Ref. 12 at 0.41 K, and the theoretical curve is given by the lowest breather excitation at zero temperature. This figure is taken from Ref. 4. © (1999) American Physical Society.

$\alpha(H/T)^2$ clearly dominates the linewidth. The shift of the resonance field also follows the theoretical proposal [Eq. (5)] as shown in Fig. 3(b). On the other hand, the breather ESR linewidth shows a completely different T dependence, that is, the rapid decrease in linewidth as T is decreased below the crossover regime as shown in Fig. 3(a). For the gapped breather regime, the magnetic excitation is dominated by the particle-like breather excitation. Therefore, the ESR linewidth is governed by the lifetime, which is limited by collisions between thermally excited particles. Since the number of excited particles decreases exponentially toward $T = 0$, the linewidth is expected as $\delta H \propto \exp[-E_g(H)/T]$, which is represented by the dashed lines in Fig. 3(a), where $E_g(H)$ is obtained from Fig. 4. The field dependence of the first-breather ESR line at $T = 0.5\,\mathrm{K}$ is plotted for different field orientations in the inset of Fig. 4. As this field dependence corresponds to Eq. (4) as shown by the OA theory, $E_g(H)$ can be calculated from the experimental data using Eq. (4) without any adjustable parameters. The obtained $E_g(H)$ for $H \,//\, c$ in Fig. 4 clearly obeys the relation $E_g(H) \propto H^{2/3}$ suggested by the OA theory while it shows that the induced gap for $H \,//\, a$ or $H \,//\, b$ is not sufficiently large to satisfy the condition as $k_B T \ll E_g(H)$ even at 0.5 K.

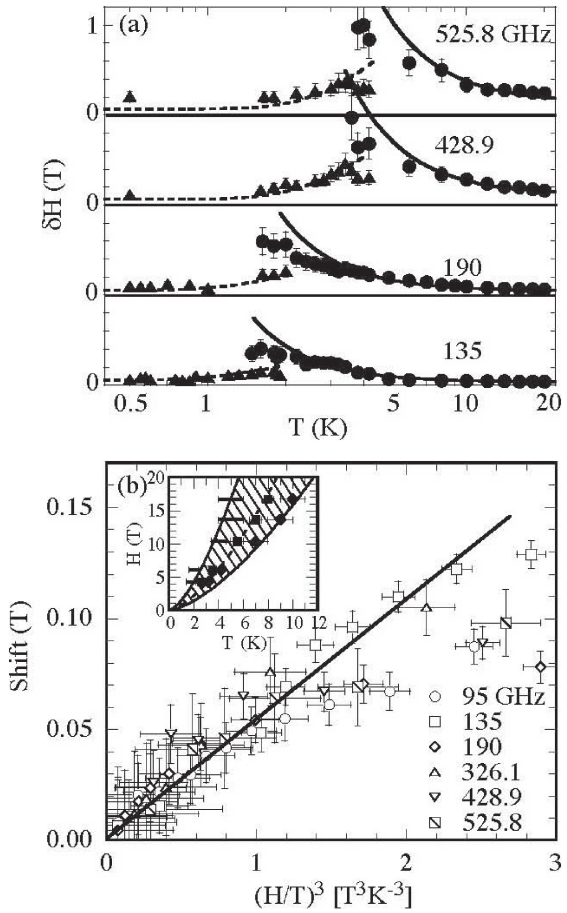

Fig. 3. (a) Temperature dependence of the linewidth δH, defined as full width at the half maximum, for the spinon ESR line (solid circles) and the first breather ESR line (solid triangles) observed for Cu benzoate. The solid line represents the function $\alpha(H/T)^2$ [Eq. (6)] plus a small contribution βH, whereas the dashed line represents the function $\exp(-E_g(H)/T)$, where $E_g(H)$ is taken from Fig. 4. (b) Resonance field shift is plotted against $(H/T)^3$ [Eq. (5)]. In the inset, the solid squares and diamonds represent the onset of the deviation from the formulas for the spinon regime in δH and in the shift, respectively. The solid line in the inset is an eye guide. The thick horizontal bars represent the crossover regime, where the spinon and breather ESR lines coexist. The dashed line is the curve of $k_B T = E_g(H)$, where $E_g(H)$ is taken from Fig. 4. This figure is taken from Ref. 14. © (2000) American Physical Society.

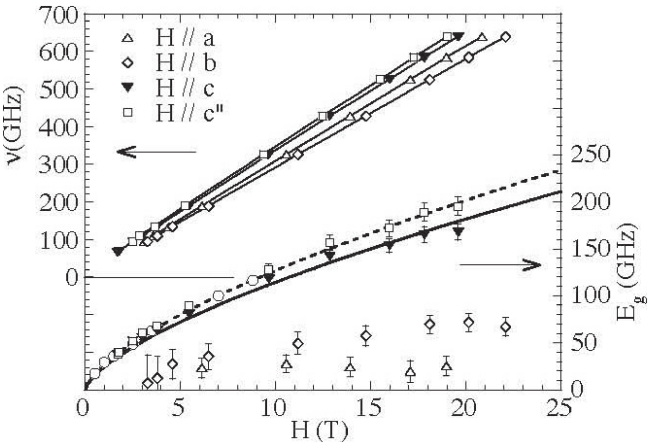

Fig. 4. In the inset, a frequency-field plot of the main ESR line for different field orientations in Cu benzoate is shown. The solid lines are eye guides. The main panel shows the plot of $E_g(H)$ as a function of external field. Here, the open circles show the value determined by the specific heat measurements taken from Ref. 13. The dashed and solid lines are the theoretical curves of $E_g(H) \propto H^{2/3}$. The c''-axis is in the ac-plane and tilts 21° from the a-axis. This figure is taken from Ref. 14. © (2000) American Physical Society.

To conclude, the validities of i) and ii) suggested by the OA theory were confirmed in a very wide-field range for Cu benzoate from the ESR experiments of Asano et al.[14] The relations i) and ii) were also confirmed by high-frequency ESR measurements in other $S = 1/2$ antiferromagnetic chain systems, such as copper pyrimidine dinitrate (Cu-PM, $J = 36$ K),[15,16] $KCuGaF_6$ ($J = 103$ K),[17] and $BaCu_2(Si_{1-x}Ge_x)_2O_7$,[18] where the interchain interaction is canceled at $x = 0.65$ ($J = 479$ K). In particular, soliton and higher order breather modes together with some "unknown modes", whose origins were unclear at the moment, were observed in Cu-PM[15] and $KCuGaF_6$[17] by taking advantage of an intrachain exchange interaction J much larger than that of Cu benzoate. Furuya and Oshikawa developed a boundary field theory approach to ESR in open $S = 1/2$ Heisenberg antiferromagnetic chains with an effective staggered field.[19] They suggested that several "unknown modes" found in ESR experiments on $KCuGaF_6$ and Cu-PM can be understood as boundary resonances related to the existence of boundary-bound states (BBS) of elementary excitations and the modification of the selection rules at the boundary, which will be introduced by the sine-Gordon effective field theory with boundaries. The example of $KCuGaF_6$ is shown in Fig. 5.[19] Moreover, as the relation $E_g(H) \propto H^{2/3}$ in i) is only valid in the low-magnetic-field region, Zhao et al. showed that the energy gap of the first breather is a nonmonotonic function of the field, and it presents a minimum around the saturation field before the linear increase above saturation based on the density matrix renormalization group (DMRG) numerical simulation.[20] This prediction was confirmed in the vicinity of the saturation field ($H_{sat} = 27$ T) in Cu benzoate[21] as shown in Fig. 6 and also in Cu-PM[24] using the pulsed high magnetic field ESR.

Another contribution to the linewidth, which is approximately T-linear and frequency-independent behavior denoted by Eq. (7) for the temperature region $T \ll J$, was also obtained by the OA field theory approach.[5] This behavior of the linewidth is due to an exchange anisotropy, and it is observed in many quasi-1D $S = 1/2$ antiferromagnets,[25–30] including $KCuF_3$, $CuGeO_3$, and NaV_2O_5 as shown in Fig. 7.

2.2 *ESR in 1D antiferromagnet with uniform DMI*

Cs_2CuCl_4 is considered as a frustrated $S = 1/2$ quasi-2D distorted triangular lattice antiferromagnet in the bc-plane, but it orders into a helical incommensurate state at $T_N = 0.62$ K.[31] However, the spin-liquid phase in the 1D antiferromagnetic chain along the b-axis was discussed by ESR[8] in the temperature region $T_N < T < T_{CW} = 4$ K, where T_{CW} stands for the Curie–Weiss temperature. Although it is a quasi-2D system, it is associated with the effective decoupling of spin chains with the intrachain exchange J due to the frustration of interchain couplings $J' = 0.34J$ along lateral sides of the triangle. Povarov et al.[8] observed the splitting of ESR at 1.3 K in the cases of H // a, c as shown in Fig. 8. They considered the Hamiltonian containing the intrachain exchange J along the b-axis, the uniform DMI, where the crystal structure forbids the DM component along the b-axis,

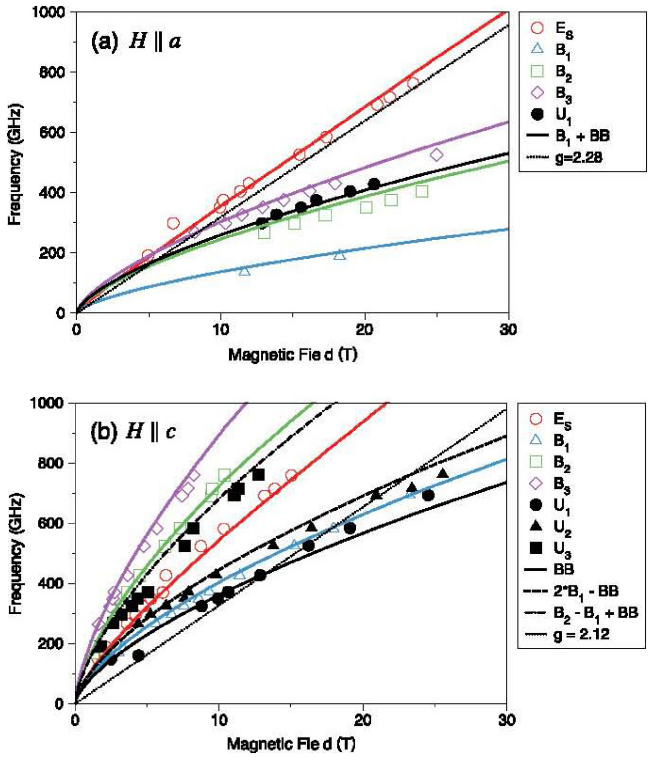

Fig. 5. (Color online) Frequency-field diagrams of ESR in $KCuGaF_6$[17] for (a) $H \,//\, a$ and (b) $H \,//\, c$ configurations. The dotted line is the high-temperature paramagnetic resonance. The open and filled symbols represent bulk and "unknown" modes, respectively. E_s, B_1, B_2, and B_3 denote resonances $\omega = E_s$, M_1, M_2, and M_3 by a soliton S and breathers B_n, respectively. An antisoliton $\bar{S}$ also leads to $\omega = E_s$. The labels U1, U2, and U3 are "unknown" peaks found in Ref. 17. (a) The configuration $H \,//\, a$ bears the smallest $h = c_s H$ with the coefficient $c_s = 0.031$. An excitation $\omega = M_1 + M_{BBS}$ is found in addition to the bulk excitations. (b) The configuration $H \,//\, c$ bears the largest staggered field with $c_s = 0.178$. This large c_s makes the rich kinds of boundary mode detectable. The labels BB, 2^*B_1–BB, and B_2–B_1+BB denote $\omega = M_{BBS}$, $2M_1 - M_{BBS}$, and $M_2 - M_1 + M_{BBS}$, respectively. This figure is taken from Ref. 19. © (2012) American Physical Society.

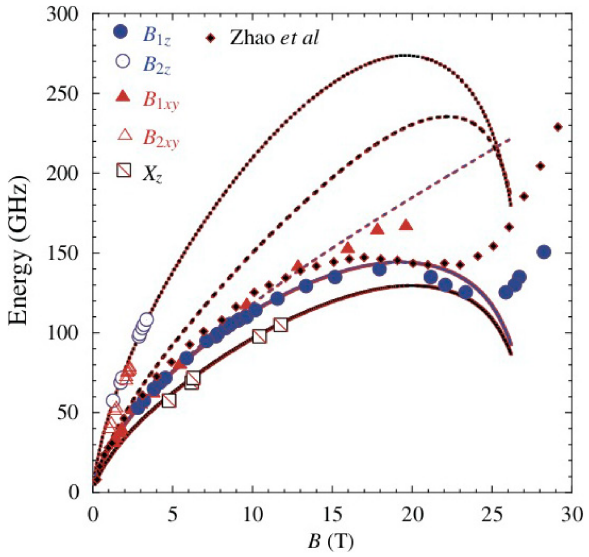

Fig. 6. (Color online) Frequency-field diagram of Cu benzoate up to 30 T. The mode above the saturation field is also marked as B_{1z}, although the nature of the excitation is different from the B_{1z} observed below the saturation. X_z is assigned to the transition between B_{1z} and B_{2z}. The diamonds show the result of the DMRG calculation for the c-axis.[20] The dotted black, dashed black, solid blue, and solid black curves are the second breather B_2, soliton, first breather B_1, and inter-breather B_2–B_1 excitations, respectively, which are calculated using Eq. (3)[22] in Ref. 21. The dashed blue curve is the B_1 calculated using Eq. (2)[23] in Ref. 21. All theoretical curves are plotted up to $0.97H_s$, where H_s is the saturation field. This figure is taken from Ref. 21. © (2006) IOP Publishing Ltd and Deutsche Physikalische Gesellschaft.

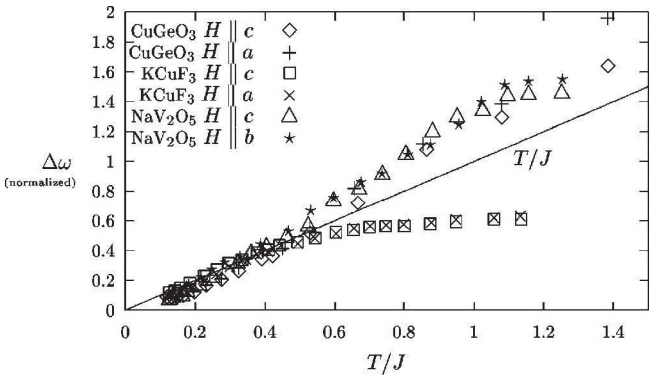

Fig. 7. Temperature dependence of ESR linewidth in $KCuF_3$, $CuGeO_3$, and NaV_2O_5. The data are from Refs. 28, 29, and 30, respectively. The horizontal axis is the temperature T normalized by the exchange coupling J, and the vertical axis is the normalized linewidth. This figure is taken from Ref. 5. © (2002) American Physical Society.

and the Zeeman term. Then, the DMI can be gauged away from the Hamiltonian by the position-dependent rotation of the angle $\tan(\alpha) = -D/J$,[8,32] and to the linear order in D/J, the ESR response of this model coincides with that of an isotropic Heisenberg chain.[5] Considering the ESR absorption from the transverse structure factor of the chain, the splitting of the ESR lines into two at the Γ point as

$$h\nu_{\pm} = |g\mu_B H \pm \pi D/2| \tag{8}$$

is obtained for $\mathbf{H} \,//\, \mathbf{D}$, and it is schematically interpreted in Fig. 9.[8] This result is also consistent with Fig. 8. A similar splitting of ESR is also observed and discussed at 0.5 K and $\mathbf{H} \,//\, \mathbf{D}$ for a very typical quasi-1D $S = 1/2$ antiferromagnetic chain single crystal $K_2CuSO_4Br_2$, which has $T_N = 70$ mK and $T_{CW} = 20$ K, and the chain along the a-axis.[33] The typical ESR result observed at 0.5 K is shown in Fig. 10, and it can be interpreted using Eq. (8) with $D = 0.27$ K at a low magnetic field, which is along the b-axis. However, the deviation from Eq. (8) was notable in Fig. 10 at a high magnetic field. Recently, Povarov et al.[34] have suggested that this deviation at a high magnetic field can be interpreted by considering the interacting spinon liquid instead of the Fermi gas [Eq. (8)], which was suggested by the recent interacting spinon theory[35] including the backscattering interaction. Moreover, a similar splitting of ESR was also observed for $H \,//\, b$ ($\mathbf{D}$ direction of the uniform DMI) at 1.8 K in the quasi-1D $S = 1/2$ antiferromagnetic chain single-crystal $Na_2CuSO_4Cl_2$ with the intrachain exchange interaction $J = 14.2$ K along the a-axis and $T_N = 0.54$ K.[36] The estimated $D = 1.01$ K from Eq. (8) is obtained by ESR fitting, and it seems to be acceptable with the estimated $D = 1.63$ K from Eq. (2) using the observed g-values $g_a = 2.07$, $g_b = 2.23$, and $g_c = 1.99$.[36] These examples show that the fine details of spin excitation spectra at small momenta studied by ESR are strongly affected by the uniform DMI in the 1D $S = 1/2$ antiferromagnetic chain.

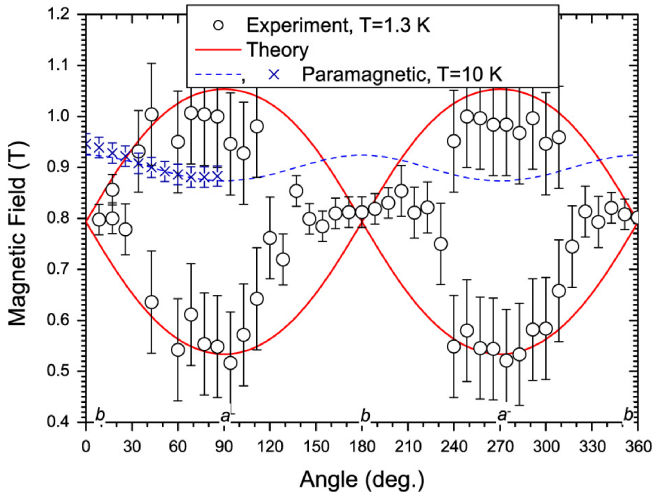

Fig. 8. (Color online) Angular dependence of resonance field in *ab*-plane of Cs_2CuCl_4 for $\nu = 27$ GHz at $T = 1.3$ K. The solid line is the theoretical prediction with $D_a/(4\hbar) = 8$ and $D_c/(4\hbar) = 11$ GHz. The observed resonance fields in the paramagnetic phase (at $T = 10$ K) are indicated by crosses; the dashed line is a theoretical fit of a paramagnetic resonance. This figure is taken from Ref. 8. © (2011) American Physical Society.

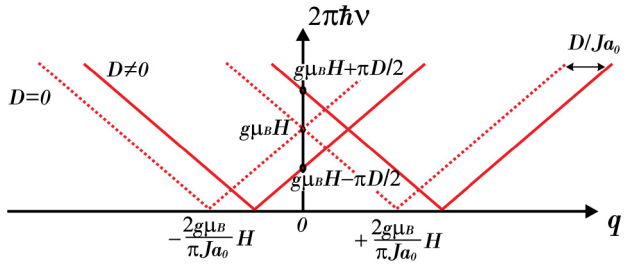

Fig. 9. (Color online) Spinon spectrum of $S = 1/2$ Heisenberg chain for $q \sim 0$ with (solid lines) and without (dashed lines) DMI. When $H \parallel D$, the momentum is boosted by $q = D/Ja_0$, where a_0 is the lattice spacing. This figure is taken from Ref. 8. © (2011) American Physical Society.

DMI in Cs_2CuCl_4 has another unique effect on ESR. The exchange paths in the *bc*-plane are shown in Fig. 11(a), and the exchange Hamiltonian of the system can be described by the exchange interactions J and J'. Two ESR modes A and B were observed at low temperatures as shown in Fig. 12.[37] Mode A corresponds to the collective excitation of spins with the frequency $\omega_A \sim g_b\mu_B H/\hbar$ for $H \parallel b$ above $H_{sat} = 8.89$ T and can be interpreted as uniform $\mathbf{k} = 0$ precession of spins around the field direction, whereas the much weaker mode B appears at $H > H_{sat}$, which can be described empirically as $\hbar\omega_B = g_b\mu_B H - \Delta_B$. Therefore, $\Delta_B/(2\pi\hbar) = 119.0$ GHz ($\Delta_B/k_B = 5.71$ K) is obtained from the ESR results in Fig. 12. Zvyagin et al.[37] discussed the origin of mode B at $H > H_{sat}$. They suggested that the reduced translational symmetry of the copper layers in Cs_2CuCl_4 by the staggered DM vectors[38] leads to the folding of the Brillouin zone of a simple triangular Bravais lattice as shown in Fig. 11(b). As a result, the ESR transitions are allowed not only for $\mathbf{k} = 0$ (mode A) but also for $k_c = 2\pi/c$ (mode B). Then, considering the dispersion of the magnetic excitations for the $S = 1/2$ antiferromagnet in the saturated phase, they came up with a simple result, that is, the difference between the excitation energies of modes A and B [Fig. 11(b)] is equal to

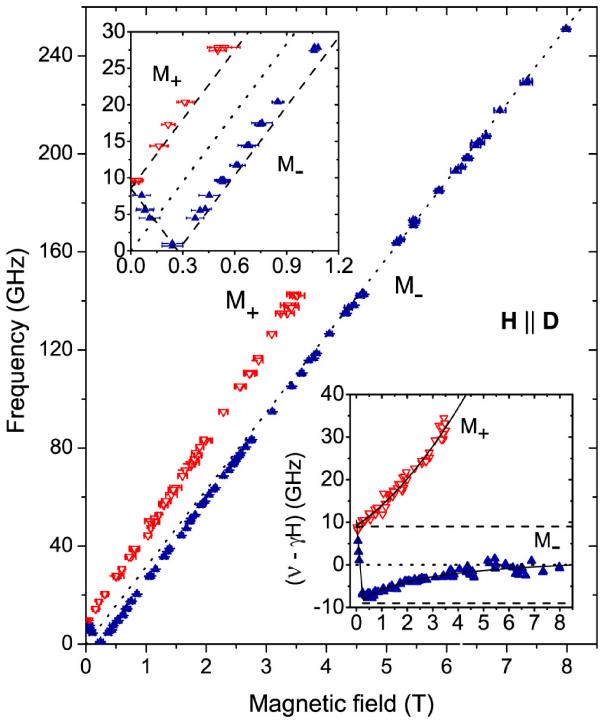

Fig. 10. (Color online) Main panel: frequency-field diagram of $K_2CuSO_4Br_2$ for $\mathbf{H} \parallel \mathbf{D}$ at 0.5 K. The dotted line represents the paramagnetic resonance. Upper inset: low-frequency part of frequency-field diagram. The dashed lines present the theoretical prediction (8) for $D = 0.27$ K. Lower inset: resonance shift from the paramagnetic frequency for $H \parallel b$ at $T = 0.5$ K. The dashed lines are drawn according to the theoretical prediction (8) for $D = 0.27$ K. The solid lines are guides to the eye. This figure is taken from Ref. 33. © (2015) American Physical Society.

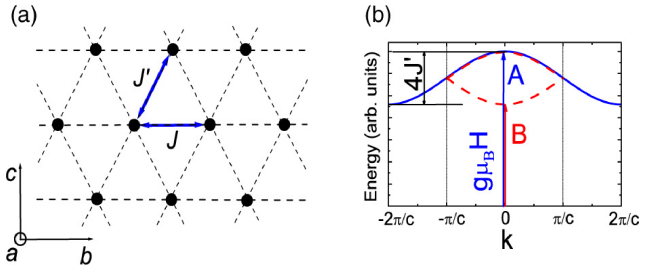

Fig. 11. (Color online) (a) Schematic of exchange paths in *bc*-plane of Cs_2CuCl_4. (b) Dispersion of magnon excitations for a $S = 1/2$ Heisenberg antiferromagnet with triangular lattice in saturated phase for an arbitrary magnetic field. The solid blue line is the dispersion of magnon excitation in the exchange approximation. The magnon dispersion within the folded Brillouin zone is shown by the dashed red line. Arrows A and B correspond to the observed ESR transitions. This figure is taken from Ref. 37. © (2014) American Physical Society.

$$\Delta\omega = \Delta_B = 4J', \tag{9}$$

which gives $J'/k_B = 1.42$ K. Knowing J', J can be determined from the saturation field using the expression

$$g_b\mu_B H_{sat} = 2J(1 + J'/2J)^2, \tag{10}$$

which gives $J/k_B = 4.7$ K ($J'/J = 0.30$). These values obtained from the ESR results are in good agreement with the estimated values $J/k_B = 4.34$ K, $J'/k_B = 1.48$ K, and $J'/J = 0.34$[39] from the neutron scattering experiments in the saturated phase. Therefore, owing to the very peculiar DMI in Cs_2CuCl_4, the observation of ESR modes above H_{sat} and the

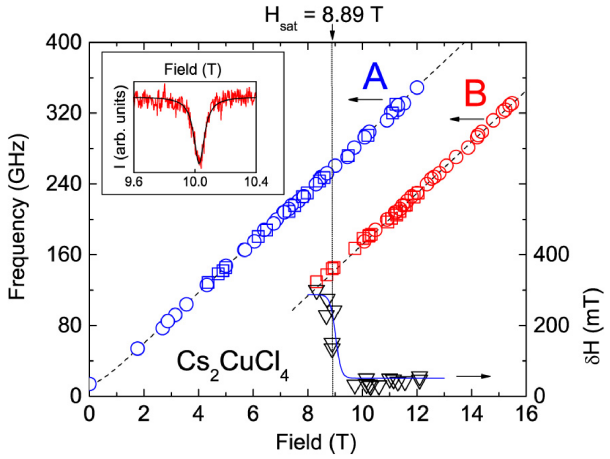

Fig. 12. (Color online) Frequency-field diagram of ESR excitations in Cs_2CuCl_4 measured at 0.5 K (squares) and 1.5 K (circles for H // b). The dashed lines correspond to fit results. The linewidth of mode B vs field is shown by triangles; the solid line is a guide for the eye. The inset shows an example of the ESR spectrum (mode B) taken at 178.3 GHz (T = 0.53 K); the solid line corresponds to a Lorentzian fit. This figure is taken from Ref. 37. © (2014) American Physical Society.

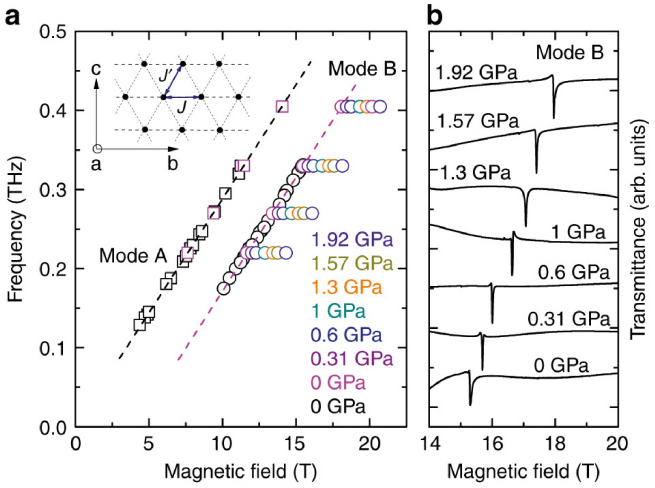

Fig. 13. (Color online) Pressure dependence of ESR excitations in Cs_2CuCl_4 (T = 1.9 K, H // b). (a) Frequency-field diagrams of ESR excitations at different pressures. The data denoted in black are taken from Ref. 37 (T = 1.5 K, 0 GPa). The dashed lines correspond to the fit results. The inset shows a schematic of magnetic sites and exchange couplings in a triangular layer of Cs_2CuCl_4. (b) ESR spectra (mode B) taken at 330 GHz at different pressures (the spectra are offset for clarity). This figure is taken from Ref. 40. © (2019) The Author(s).

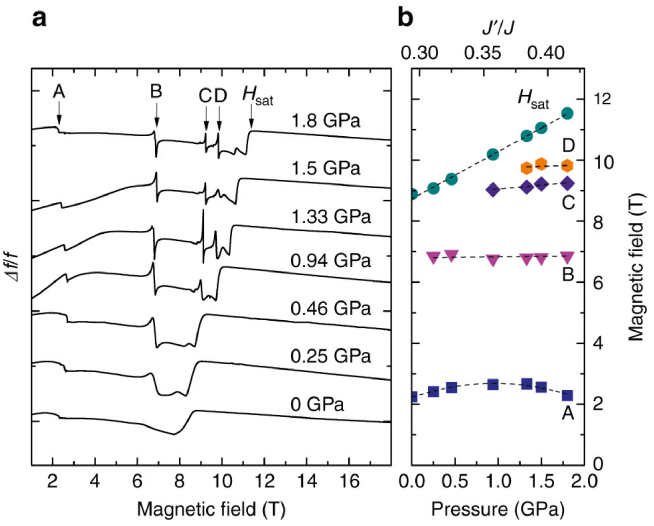

Fig. 14. (Color online) Pressure evolution of magnetic properties of Cs_2CuCl_4 obtained by TDO technique (T = 350 mK, H // b). (a) Pressure dependence of TDO frequency changes $\Delta f/f$ in response to magnetic field (the data are offset for clarity). (b) Dependences of TDO frequency anomalies on applied pressure. The calculated exchange coupling ratio J'/J is shown on the top scale. Lines are guides for the eye. This figure is taken from Ref. 40. © (2019) The Author(s).

determination of H_{sat} by magnetization measurement will be a very precise and easy method in comparison with the neutron measurement to determine J and J' in Cs_2CuCl_4. Using this advantage, the pressure dependences of J and J' in Cs_2CuCl_4 are studied with a high-pressure THz ESR system[40] installed at the High Field Laboratory at Tohoku University using the hybrid transmission-type pressure cell developed at Kobe University[41] and the 25 T cryogen-free superconducting magnet developed at Tohoku University.[42] Figure 13 shows the pressure dependence of ESR excitations in Cs_2CuCl_4 (T = 1.9 K, H // b). A clear shift of mode B is observed by applying pressure. J' is precisely determined using Eq. (9). J' increased linearly and showed a significant, almost 70%, increase at 1.92 GPa.[40] A linear increase in H_{sat} with pressure was also observed by a tunnel-diode-oscillator (TDO) technique as shown in Fig. 14. J is determined using Eq. (10) and the obtained H_{sat} and J', and the empirical equation $J'/J = 0.294 + 0.067P$, where P is the applied pressure (GPa), is obtained. For 1.8 GPa, the obtained values are $J'/k\mathrm{B} = 2.28$ K, $J/k\mathrm{B} = 5.47$ K, and $J'/J = 0.42$, indicating a 40% increase in J'/J ratio. Moreover, new magnetic phase transitions C and D under pressure were observed as shown in Fig. 14. These anomalies are speculated as transitions into the double- and single-cone phases, respectively;[40] theoretical confirmation using the precisely determined J and J' in the $S = 1/2$ distorted triangular lattice antiferromagnet is required.

2.3 *Singlet–triplet ESR transitions in quantum spin systems*

Considering the isolated $S = 1/2$ antiferromagnetic dimer, the energy levels will split into the ground singlet and excited triplet states, whose energy splitting is called the spin gap. In principle, the direct ESR transition between the singlet and triplet states is forbidden because the transition probability between these states is zero for the magnetic dipole transition from the fundamental quantum mechanical discussion, which comes from the conservation of the total spin quantum number. However, in real magnetic systems, many such direct ESR transitions are observed owing to the interactions discussed below, including inter-dimer exchange interactions, and these observed direct ESR transitions will give clear direct information to understand the energy structures in the quantum-gapped spin systems. Moreover, these inter-dimer interactions give rise to the field induced magnetic ordered state, in other words, the Bose–Einstein condensation of magnons.[43] For instance, the direct ESR transition between the singlet and triplet states is observed in the $S = 1$ 1D Haldane system $Ni(C_2H_8N_2)_2NO_2ClO_4$ (NENP),[44] non-organic spin-Peierls system $CuGeO_3$,[45] spin-dimer systems $TlCuCl_3$ and $KCuCl_3$,[46] distorted diamond chain

antiferromagnet $Cu_3(CO_3)_2(OH)_2$ (Azurite),[47] quasi-1D spin gap system $Cu_2Cl_4{\cdot}H_8C_4SO_2$,[48] and 2D orthogonal dimer or Shastry–Sutherland model substance $Sr_2(BO_3)_2$,[49] by high-frequency ESR measurements.

The detailed mechanism of the observed singlet–triplet ESR transition has not yet been totally understood for each system. However, there are at least three proposed models to interpret the observed ESR results. They are

1) the magnetic dipole transition due to the mixing of the singlet and triplet states by DMI or staggered magnetic fields,[50,51]
2) the electric dipole transition coming from a dynamical DMI induced by the ac electric field,[52] which is based on the recent discussions of spin-driven ferroelectricity in magnetoelectric multiferroic materials related to the vector spin chirality,[53–55] and
3) a phonon-assisted mechanism for the electric dipole transition.[56,57]

Some examples on models 1) and 2) will be discussed in the following.

First, we will talk about model 1). Since Haldane predicted[58] that 1D integral-S Heisenberg antiferromagnets have a gap in the excitation spectrum, it has been supported by many theoretical and experimental studies. In particular, $Ni(C_2H_8N_2)_2NO_2(ClO_4)$, abbreviated as NENP, is considered as a typical material of the 1D $S = 1$ Heisenberg antiferromagnet, the Haldane chain.[59,60] Considering the field dependence of the gap in NENP observed by ESR measurement,[44] Sakai and Shiba numerically calculated the field dependences of the energy and wave function of the ground and first excited states of the 1D $S = 1$ antiferromagnetic Heisenberg Hamiltonian with a transverse staggered field.[50] They used the exact diagonalization based on the Lanczos algorithm up to the system size N = 14. They showed that the staggered field made the ESR absorption possible from the ground state at $k = 0$ to the lowest excited state $k = \pi$ in NENP. Their results qualitatively agree with the ESR, NMR, and heat capacity measurement results, and they can explain especially the field dependences of the energy gap and intensity of ESR. This is the first suggestion that the staggered field can be the origin of the direct transition. In the case of NENP, the origin of the staggered field is considered as the alternate in the inclination of the g-tensor of the Ni^{2+} ions, which was revealed by NMR measurement.[61]

Now, we talk about Sakai's selection rule of DMI. The direct singlet–triplet ESR transition was observed[45] for the inorganic compound $CuGeO_3$ in the spin Peierls phase.[62] As DMI was proposed as a possible origin of the direct transition,[63] Sakai et al. calculated and discussed the selection rules related to DMI and its application to the spin Peierls compound $CuGeO_3$.[64] Considering two antiferromagnetically coupled $S = 1/2$ spins system

$$\mathcal{H} = J\boldsymbol{S}_1 \cdot \boldsymbol{S}_2 + \mathbf{D} \cdot (\boldsymbol{S}_1 \times \boldsymbol{S}_2) - \mathbf{H} \cdot (\boldsymbol{S}_1 + \boldsymbol{S}_2), \qquad (11)$$

the following selection rules can be obtained.[65] Here, J, $\mathbf{D}$, and $\mathbf{H}$ are the exchange interaction, D vector, and external magnetic field, respectively.

(DM-1) $\mathbf{h}(t) \perp \mathbf{H} \,//\, \mathbf{D}$: I independent of H
(DM-2) $\mathbf{h}(t) \,//\, \mathbf{H} \perp \mathbf{D}$: I dependent on H
(DM-3) $\mathbf{h}(t) \,//\, \mathbf{H} \,//\, \mathbf{D}$: I = zero

Table I. Selection rules for DMI in the case of $D^x = D^y = 0$ and $D^z \neq 0$. This table is taken from Ref. 65. © (2020) Springer-Verlag GmbH Austria.

	$\boldsymbol{H} \,//\, x$	$\boldsymbol{H} \,//\, y$	$\boldsymbol{H} \,//\, z$
$\boldsymbol{k} \,//\, x$	0	D	I
$\boldsymbol{k} \,//\, y$	D	0	I
$\boldsymbol{k} \,//\, z$	D	D	I

"D" means the finite intensity dependent on H.
"I" means the finite intensity independent of H.
"0" means no intensity.

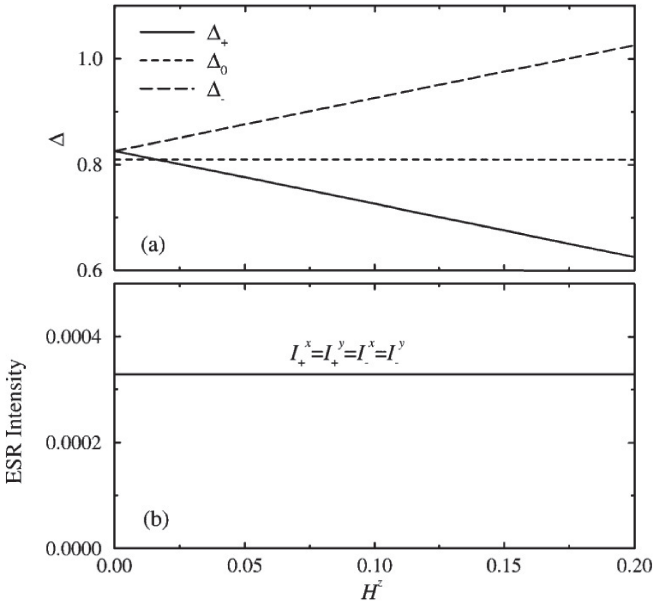

Fig. 15. (a) Energy gaps and (b) ESR intensities plotted versus external magnetic field parallel to intrachain DM vector ($D \,//\, H \,//\, z$, $D^x = D^y = 0$, and $D^z \neq 0$). I^α is the intensity for $h(t) \,//\, \alpha$. This figure is taken from Ref. 64. © (2000) The Physical Society of Japan.

Here, $\mathbf{h}(t)$ is the magnetic field component of the electro-magnetic wave. These selection rules can be modified to experimental configurations as follows. Here, the wave vector of the electro-magnetic wave k is always $\mathbf{k} \perp \mathbf{h}(t)$.

(DM-A) Faraday configuration: $\mathbf{k} \,//\, \mathbf{H}$
$I^x_{(F)} : I^y_{(F)} : I^z_{(F)} = (D^x)^2 : (D^y)^2 : (D^z)^2$
$I^a_{(F)}$: Direct ESR intensity for $\mathbf{H} \,//\, a$
(DM-B) Voigt configuration: $\mathbf{k} \perp \mathbf{H}$
(a) $\mathbf{H} \,//\, \mathbf{D}$ [rule (DM-1 or 3)]: I independent of H
(b) $\mathbf{H} \perp \mathbf{D}$ [rule (DM-2)]: I dependent on H

These selection rules are summarized in Table I. Considering $CuGeO_3$, Sakai et al. made the numerical diagonalization calculation on the cluster of 16 $S = 1/2$ spins with DMI and the alternated intrachain exchange interactions reflecting the spin Peierls distortion.[64] Figures 15 and 16 show the calculated results in the case of intrachain DMI of $D^x = D^y = 0$ and $D^z \neq 0$.[64] The calculated results considering only DMI are qualitatively consistent with the selection rules for the experimental configuration discussed above for the two coupled $S = 1/2$ spins system. The calculated ESR intensities were discussed with the experimental ESR intensities, which are summarized in Tables II and III.[51,64] As a result, D^z seems to play a dominant role in the ESR intensities with a small contribution of D^x considering the diagonal part in both tables. However, the inclusion of the

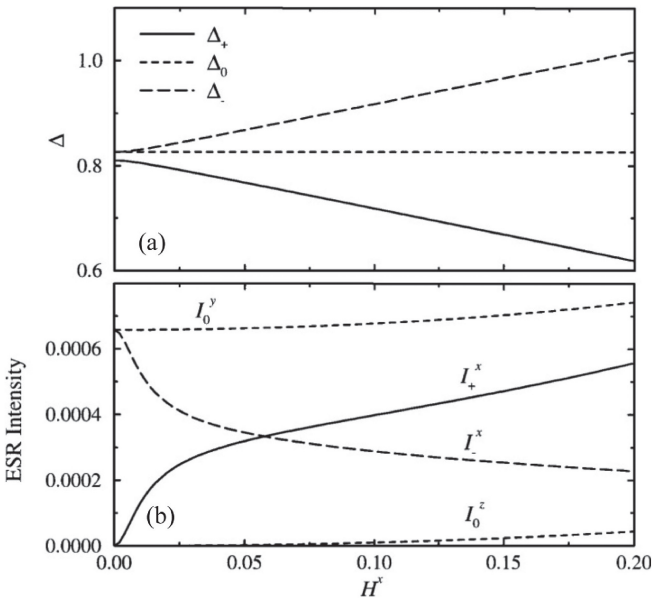

Fig. 16. (a) Energy gaps and (b) ESR intensities plotted versus external magnetic field perpendicular to intrachain DM vector (D // H // z, $D^x = D^y = 0$, and $D^z \neq 0$). I^α is the intensity for $h(t)$ // α. This figure is taken from Ref. 64. © (2000) The Physical Society of Japan.

Table II. Numerical result of ESR intensity for direct transition between ground and first excited states obtained by Sakai.[51] The x-, y-, and z-axes correspond to the a-, b-, and c-axes of $CuGeO_3$, respectively. S, M, and W denote that the intensity of the transition is strong, moderate, and weak, respectively. This table is taken from Ref. 51. © (2003) The Physical Society of Japan.

Polarization	H // x	H // y	H // z
k // x	M	M	M
k // y	S	W	M
k // z	S	M	S

Table III. Experimental result of ESR intensity for direct transition between ground and first excited states, which was observed in the measurement on $CuGeO_3$ by Nojiri et al.[45] This table is taken from Ref. 51. © (2003) The Physical Society of Japan.

Polarization	H // a	H // b	H // c
k // a	M	M	M
k // b	M	W	S
k // c	S	W	S

staggered field by the alternation in the inclination of the g-tensor of the Cu^{2+} ions is really required to interpret the off-diagonal part of the experimental Table III in comparison with Table II.[51] Therefore, $CuGeO_3$ seems to be not an ideal system to discuss the direct transition only on the basis of DMI and further detailed study is required. On the other hand, the quasi-1D spin gap system $Cu_2Cl_4{\cdot}H_8C_4SO_2$[48] may be a good example of the DM rule (DM-A). $Cu_2Cl_4{\cdot}H_8C_4SO_2$ is an $S = 1/2$ alternating AF chain ($J'/J = 0.98$, $J = 105.6$ K) with a spin gap of about 160 GHz, which was determined by frequency-dependent ESR measurements at 1.7 K.[48] Very anisotropic ESR intensities, $I^{a*} : I^b : I^c = 1 : 0 : 5.2 \pm 0.4$, were observed under the Faraday configuration at 140 GHz and 1.7 K, and DM-rule (DM-A), $I^{a*} : I^b : I^c = (D^{a*})^2 : (D^b)^2 : (D^c)^2$, was applied. Therefore,

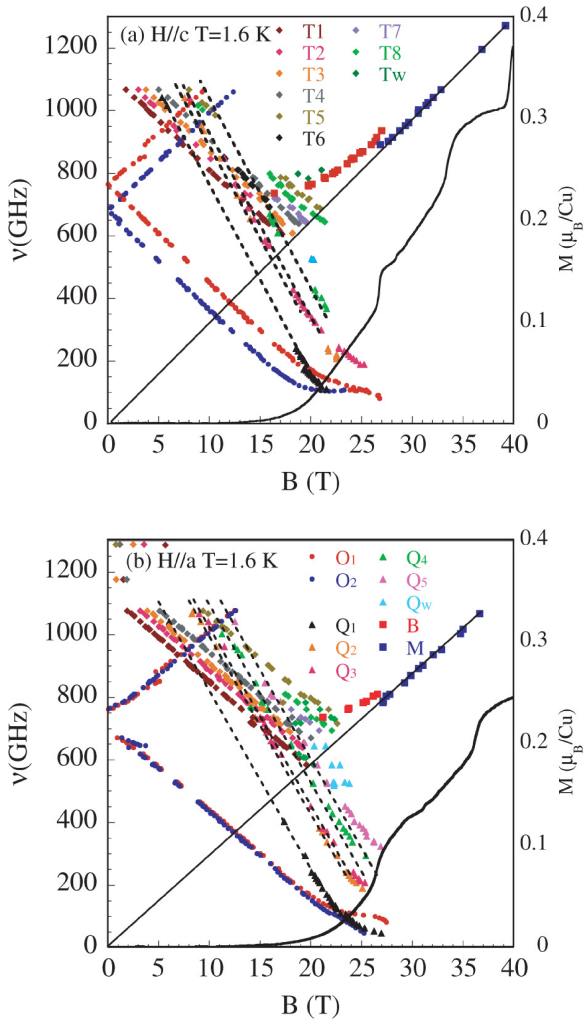

Fig. 17. (Color online) Frequency-field plot of $SrCu_2(BO_3)_2$ at 1.6 K for (a) B // c and (b) B // a. O, T, Q, B, M are one-triplet, tripletBS, quintetBS, new signal, and paramagnetic like signal, respectively. The subscript W denotes weak signals that are not well classified. The solid line shows the paramagnetic resonance line ($\nu = g\mu_B H$, ν: frequency, g: g-value). The dashed lines are eye guides. Magnetization curves taken from Ref. 68 are also plotted. This figure is taken from Ref. 49. © (2003) The Physical Society of Japan.

the ratio between the D-vector components is estimated to be $|D^{a*}| : |D^b| : |D^c| = 1.0 : 0.0 : 2.3 \pm 0.1$. The confirmation of the D-vector by other means will be an interesting issue to confirm the validity of the selection rule.

The quasi-two-dimensional (2D) orthogonal dimer compound $SrCu_2(BO_3)_2$[66] is well described by the Shastry–Sutherland model,[67] in which the complete dimer state is the exact ground state, and the spin gap between the singlet and triplet states is determined to be 722 GHz by detailed frequency-dependent ESR measurements of the direct transition as shown in Fig. 17.[49] Nojiri et al.[49] and Sakai[51] discussed the DMI in $SrCu_2(BO_3)_2$ from the selection rule of observed ESR intensities. An intradimer DMI: D_d // ab-plane, the c-axis and ab-plane components of interdimer DMI: (D_c and D_{ab}, respectively) and a staggered field, all of which are allowed to exist owing to the crystal structure of $SrCu_2(BO_3)_2$, are considered. However, D_c exists regardless of the small buckling of the edge-shared CuO_4 planes, whereas D_d and D_{ab} exist only when this buckling is taken into account. Therefore, D_d and D_{ab} are expected to be small.

For instance, neutron measurements estimate $D_c = 0.18$ meV[69] and $D_{ab} \approx 0.3D_c$.[70] Moreover, considering the large anisotropy of the g-value in the ac-plane ($g_a = 2.05$ and $g_c = 2.28$) and the small one in the ab-plane, a sizable staggered field is expected only for $H \,//\, c$. As the ESR experiments were carried out in the Faraday configuration, the DM rule (DM-A) is expected to apply. In the case of $H \,//\, c$, the ESR intensity of O_1 in Fig. 17 showed no field dependence, suggesting that D_c gives rise to the constant ESR intensity, which is consistent with the DM rule (DM-A). On the other hand, the intensity of O_2, which is much lower than that of O_1, showed a characteristic field dependence, which is not compatible with the DM rule, and its origin requires further study. In the case of $H \,//\, a$, D_d and D_{ab} have field parallel components; the field-independent intensity observed in the experiment is compatible with the DM rule. Moreover, the major contribution of D_d against D_{ab} is supported by the fact that the intensities of O_1 and O_2 are almost constant when rotating an external magnetic field within the ab-plane. Since two types of dimer are orthogonally arranged in the ab-plane, the sum of the squares of a field-parallel component of D_d over the A- and B-dimers is constant for any field direction in the plane, while this is not the case for D_{ab}. However, the observed ESR intensity is higher in $H \,//\, a$ than in $H \,//\, c$, which suggests that $D_c < D_d$ from the DM rule (DM-A). Is this acceptable for $SrCu_2(BO_3)_2$? Can we determine D_d by other means? These are the remaining issues concerning DMI for $SrCu_2(BO_3)_2$.

The ground state of the Shastry–Sutherland model is governed by the exchange ratio $\alpha = J'/J$, where J' and J are the inter- and intradimer exchange interactions, respectively. Miyahara and Ueda estimated the parameters for $SrCu_2(BO_3)_2$ as $J = 85$ K and $\alpha = 0.64$ from the theoretical calculations,[71] whereas the magnetization measurement up to 118 T using the vertical-type single-turn coil technique, which revealed the 1/2 plateau, showed good agreement with the numerical simulations using $\alpha = 0.63$.[72] Moreover, Koga and Kawakami showed the existence of the plaquette singlet phase (plaquette) between the dimer singlet phase (dimer) and the antiferromagnetic ordered phase (AF) as shown in Fig. 18.[73] Therefore, the pressure tuning of α for $SrCu_2(BO_3)_2$ has attracted considerable attention. However, as the ground state of both the dimer and plaquette phases is singlet, the magnetization measurement under pressure cannot detect the phase transition at α_{c1}. Therefore, the determination of the spin gap between the singlet and triplet states by the observation of the direct transition from THz ESR under pressure[74,75] is really required because the discontinuous first-order phase transition of the triplet state was predicted theoretically.[76] Sakurai et al.[77] observed pressure-dependent ESR signals associated with transitions from the singlet ground state to the one-triplet excited states and the two-triplet bound state for $SrCu_2(BO_3)_2$ up to 2.1 GPa. The experimentally determined gaps shown in Fig. 19 showed a clear first-order phase transition at $P_c = 1.85 \pm 0.05$ GPa,[77] and the observed spin gap in the plaquette phase was consistent with the neutron result.[79] Moreover, by comparing this pressure dependence with the calculated excitation energies obtained from an exact diagonalization, Sakurai et al. determined the precise pressure dependences for J' and J considering the DMI. This

Fig. 18. Ground state of Shastry–Sutherland model vs exchange ratio $\alpha = J'/J$, where J' and J are inter- and intra-dimer exchange interactions, respectively. This figure is modified from Ref. 73. © (2000) American Physical Society.

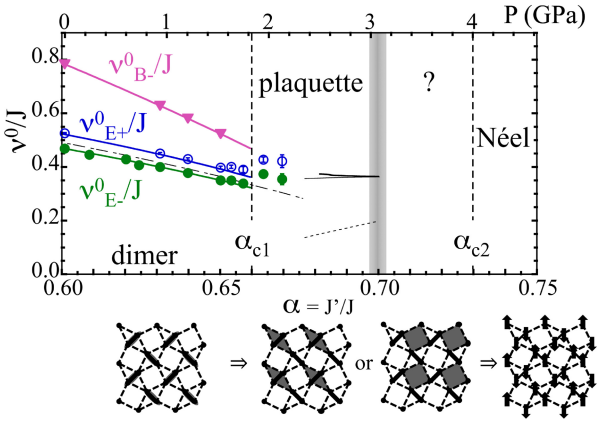

Fig. 19. (Color online) Pressure dependence of gaps from singlet ground state to one-triplet excited states and two-triplet bound state for $SrCu_2(BO_3)_2$ determined by high-pressure ESR measurements. This figure is modified from Ref. 78. © (2019) The Physical Society of Japan.

gives the experimentally determined $\alpha_{c1} = 0.660$, which is compatible with 0.677 determined theoretically (Fig. 18). This example shows how the observation of the direct transition by ESR through DMI can reveal rich physics.

Second, we will discuss model 2). An important point of this model suggested by Kimura et al.[52] is that the coupling between the electric polarization $\boldsymbol{P}$ and the ac electric field $\boldsymbol{E}^{(i)} = \boldsymbol{E}e^{-i\omega t}$ can be regarded as a dynamical DMI as follows:

$$\mathscr{H}_{PE} = \boldsymbol{P} \cdot \boldsymbol{E}e^{-i\omega t} = \boldsymbol{d} \cdot (\boldsymbol{S}_i \times \boldsymbol{S}_j)e^{-i\omega t}, \tag{12}$$

where

$$\boldsymbol{d} = \sum_{\mu,\nu} E_\nu C_{\nu\mu} \quad (\nu, \mu = x, y, z). \tag{13}$$

As the DMI term in Eq. (12) has its matrix elements between the singlet and triplet states, Eq. (12) results in a finite probability of the electric dipole transition when $\hbar\omega$ equals the energy difference between these states. To test this proposal, Kimura et al. demonstrated ESR measurements on the $KCuCl_3$ single crystal,[52] in which antiferromagnetic dimers composed of Cu^{2+} ions with spin $S = 1/2$ are coupled by weak interdimer exchange interactions, forming a three-dimensional dimer network. In such a weakly coupled dimer system, a spin triplet excited on a dimer propagates through the dimer network via the interdimer exchange interaction, which will lead to the field-induced Bose–Einstein condensation of the triplet excitation.[80] Moreover, as a spontaneous electric polarization, whose absolute value is proportional to $|\langle \boldsymbol{S}_i \times \boldsymbol{S}_j \rangle|$ in the ground state, was observed in $TlCuCl_3$,[81] which is isomorphous with $KCuCl_3$, the action

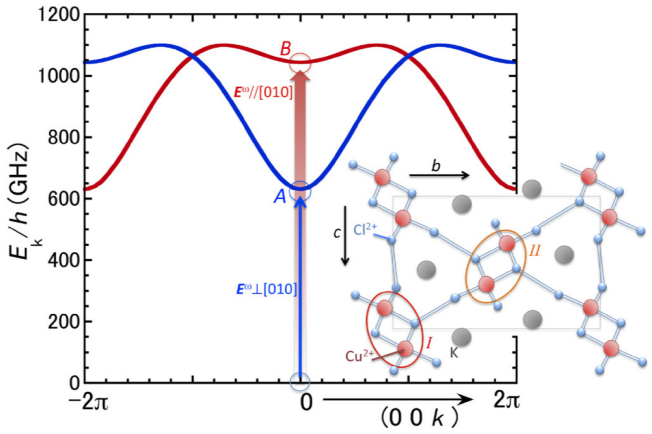

Fig. 20. (Color online) Dispersion curves of triplet excitation in $KCuCl_3$ calculated on the basis of bond operator theory. The inset shows the crystal structure of $KCuCl_3$. Two sets of triplet excitation modes are superimposed because of the presence of two types of crystallographically different dimers I and II in this compound. The singlet–triplet transitions *A* and *B* observed from the ESR measurements are excited by the ac electric field for $\boldsymbol{E}^\omega \perp [010]$ and $\boldsymbol{E}^\omega$ // [010], respectively. This figure is taken from Ref. 52. © (2018) American Physical Society.

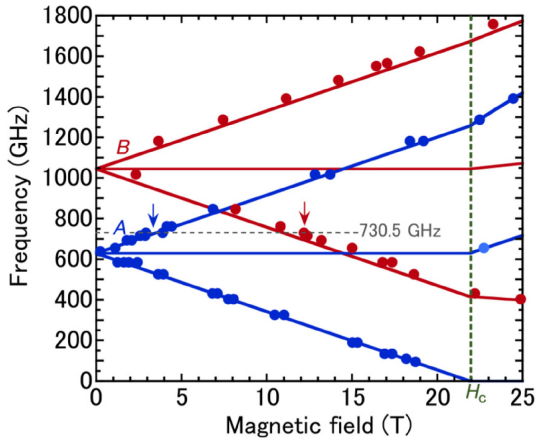

Fig. 21. (Color online) Frequency-field plot of ESR resonance fields observed in $KCuCl_3$ for H // [010]. Two sets of singlet–triplet transitions A and B are observed. This figure is taken from Ref. 52. © (2018) American Physical Society.

of $\boldsymbol{P} = \tilde{C}(\boldsymbol{S}_i \times \boldsymbol{S}_j)$ in Eq. (12) is also expected in $KCuCl_3$. Detailed polarized ESR measurements of the quantum spin dimer system $KCuCl_3$ by Kimura et al.[52] showed that the observed singlet–triplet transitions A and B in Figs. 20 and 21 are driven by ac electric fields of the electromagnetic wave through a dynamical DMI Eq. (12). As $TlCuCl_3$ is isomorphous with $KCuCl_3$, the direct ESR transition observed in $TlCuCl_3$[46] is also expected to be the electric dipole transition through the above mechanism. However, as the high-field magnetization measurement of $TlCuCl_3$ up to 100 T using the single-turn technique[82] indicated a broken particle–hole symmetry, which is expected to be symmetric in the field-induced Bose–Einstein condensation picture, detailed polarized ESR measurements of $TlCuCl_3$ may also be required to confirm the electric dipole direct transition.

Finally, one remaining issue related to DMI will be discussed. Kikuchi et al. proposed that $Cu_3(CO_3)_2(OH)_2$, which is a well-known natural mineral azurite, might be the

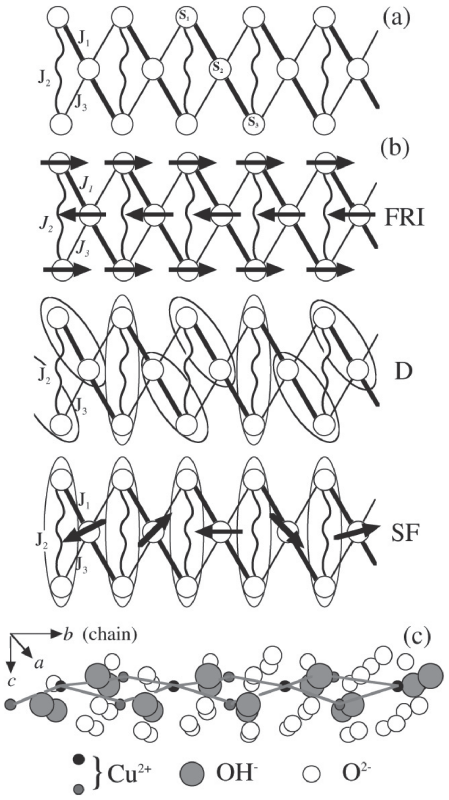

Fig. 22. (a) Schematic exchange network of distorted diamond chain model. The open circles represent $S = 1/2$ sites. (b) Schematic spin configurations of ground states for $S = 1/2$ distorted diamond chain. (c) Crystal structure of azurite, $Cu_3(CO_3)_2(OH)_2$. The *b*-axis is the chain direction. This figure is taken from Ref. 47. © (2003) The Physical Society of Japan.

first model substance for the $S = 1/2$ distorted diamond chain.[83,84] As the unit in the spin network of azurite shown in Fig. 22(a) resembles the playing card diamond shape, it is called the diamond chain. Okamoto et al.[85] and Tonegawa et al.[86] studied the ground state of the $S = 1/2$ distorted diamond chain theoretically considering the antiferromagnetic interactions J_1, J_2, and J_3 in Fig. 22(a). They determined the ground state phase diagram, composed of ferrimagnetic (FRI), dimerized (D), and spin fluid (SF) phases as schematically shown in Fig. 22(b). They also suggested that the ground state of azurite is in the SF phase considering the magnetization of azurite.[84] However, Gu and Su reported the finite temperature transfer matrix renormalization group (TMRG) method results for the $S = 1/2$ distorted diamond chain model, and they suggested that the double-peak behavior of $\chi(T)$ found in the experiment[84] cannot be reproduced by the original J_1, J_2, and J_3, but well reproduced by the very anisotropic ferromagnetic J_3 ($J_{3x}/J_{3z} = J_{3y}/J_{3z} = 1.7$).[87] Although such very anisotropic J_3 is not typical for the Cu^{2+} ion, their comment triggered various discussions and experiments published in over 300 papers, especially focused on whether the ferromagnetic exchange interaction exists because it leads to nonfrustrated or frustrated spin system. However, it seems to have been settled when Jeschke et al. introduced an effective generalized $S = 1/2$ diamond chain model with J_1, J_2, J_3, and a new Cu monomer–monomer exchange J_m.[88] With antiferromagnetic J_1, J_2, J_3, and J_m, they were able to explain a broad

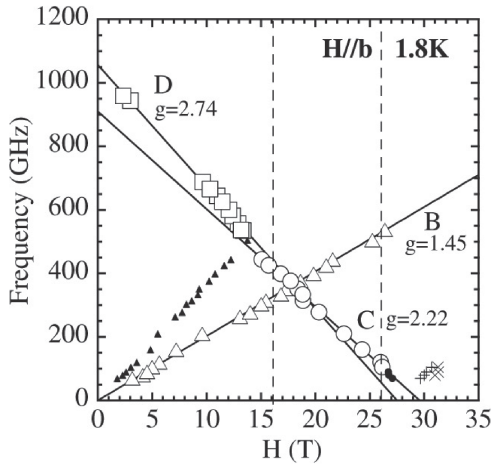

Fig. 23. Frequency-field plot of $Cu_3(CO_3)_2(OH)_2$ observed at 1.8 K for H // b. The major resonances D and B (large symbols) correspond to the direct ESR transitions of J_2 dimers and the monomer ESR, respectively. The dashed lines correspond to the critical fields of the 1/3 magnetization plateau. This figure is taken from Ref. 47. © (2003) The Physical Society of Japan.

range of experiments, including the double-peak behavior of $\chi(T)$ on azurite.[88] Therefore, azurite can be considered as a frustrated antiferromagnet. In the early stage of the research on azurite, direct transitions related to the spin gap of 1057 GHz were observed by the high-field ESR as shown in Fig. 23.[47] The observed direct ESR transitions D can be considered as coming from the J_2 dimer in a simple scheme of the SF phase because DMI can exist at the J_2 dimer from the crystallographic symmetry. On the other hand, the magnetization of azurite at 1.5 K showed a very anisotropic 1/3 plateau where plateau regions were 16–26 T for H // b and 11–30 T for $H \perp b$ as shown in Fig. 24.[84] As such a large anisotropy is unusual for the Cu^{2+} ion system without a single ion anisotropy, DMI is considered as the only possible origin where the existence of DMI is also suggested by the small slope in the 1/3 magnetization plateau shown in Fig. 24 and the observation of the direct ESR transition from the J_2 dimer. Therefore, the theoretical calculation of magnetization was performed assuming that the D vector of the DMI is perpendicular to both the J_2-dimer bond and the b-axis, on the basis of approximate crystallographic mirror planes.[84] Although the actual crystal structure of azurite is monoclinic, "approximate" comes from the fact that $\beta = 92.2°$. The calculated result can explain the anisotropic magnetization results in Fig. 24 provided that the DMI of $D = 0.3J_2$ is present in azurite.[84] Although $(\Delta g/g)J_2 = (0.06/2)J_2$[2] obtained from ESR results near room temperature[47] may be underestimated because obtained g-values are the average of two different diamond chains, $\Delta g = 0.6$ corresponding to $D = 0.3J_2$ appears very large for the typical Cu^{2+} ion. Moreover, the intensity ratio $I^a : I^b : I^c = 6 : 10 : 10$ is obtained by ESR measurement under the Faraday configuration.[89] Although two different diamond chains exist in azurite, D^b seems to be comparable to D^a and D^c by applying the selection rule (DM-A), which is in contrast to the assumption made for the magnetization calculation. In summary, the interpretation of the anisotropic 1/3 magnetization plateau observed in azurite is still a remaining issue.

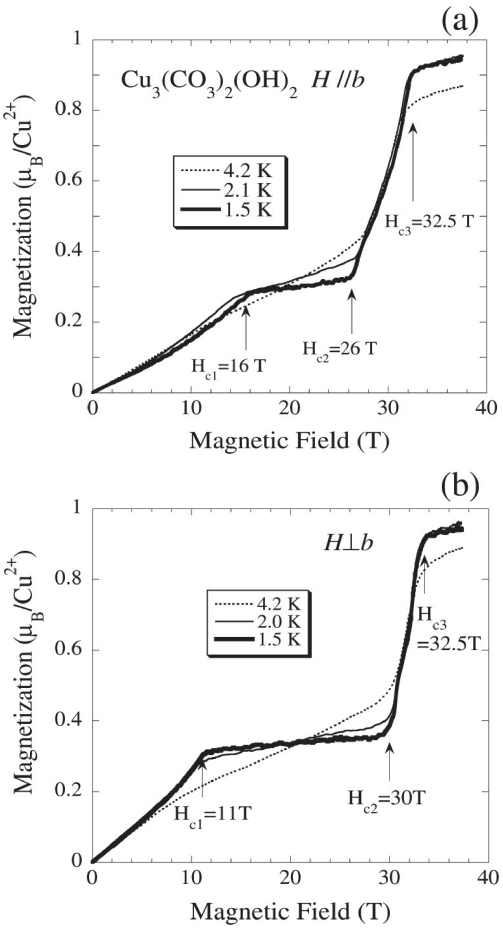

Fig. 24. High field magnetization curves of $Cu_3(CO_3)_2(OH)_2$ measured below 4.2 K. The magnetic field was applied (a) along and (b) perpendicular to the b-axis. This figure is taken from Ref. 84. © (2005) American Physical Society.

3. Exotic Quantum Spin Systems and DMI

3.1 $S = 1/2$ kagome lattice antiferromagnets: Ground state selected by DMI

As a high geometrical frustration is expected for the kagome antiferromagnet whose name "kagome" comes from the woven-bamboo pattern of the Japanese bamboo basket,[90] it has attracted considerable attention theoretically and experimentally, and it may be a good candidate for a quantum spin liquid (QSL) in the case of $S = 1/2$.[91] DMI, which is expected in the model substances of kagome lattice antiferromagnets due to the crystal symmetry, may also play an important role in determining the magnetic properties of $S = 1/2$ kagome lattice antiferromagnets. Cépas et al. discussed the role of DMI in the $S = 1/2$ kagome lattice antiferromagnet $ZnCu_3(OH)_6Cl_3$ (herbertsmithite) theoretically.[92] At that time, $ZnCu_3(OH)_6Cl_3$ attracted considerable attention as "a perfect kagome lattice".[93,94] By the exact diagonalization (ED) method up to N = 36, they suggested that the system has no magnetic moment for $D < D_c = 0.1J$ and has Néel order for $D > D_c$ as shown in Fig. 25, where D is the component of the **D** vector perpendicular to the kagome plane and J is the nearest-neighbor exchange interaction in the kagome plane.[92] To obtain a simple understanding of the occurrence of a Néel phase, a simple physical picture was given by Cépas et al. On a triangle,

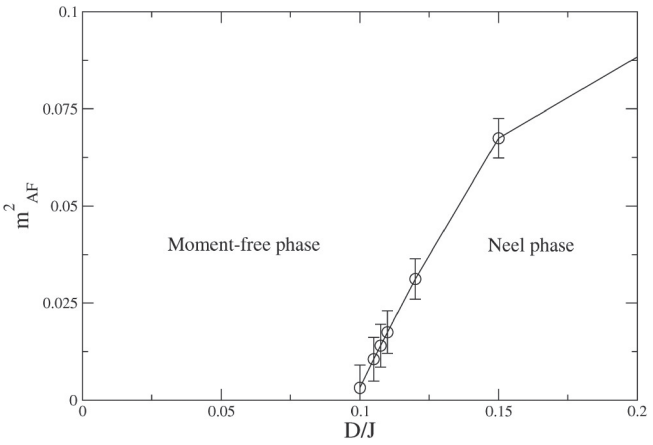

Fig. 25. Néel order parameter as a function of D/J obtained from extrapolations to infinite size in exact diagonalization calculation. This figure is taken from Ref. 92. © (2008) American Physical Society.

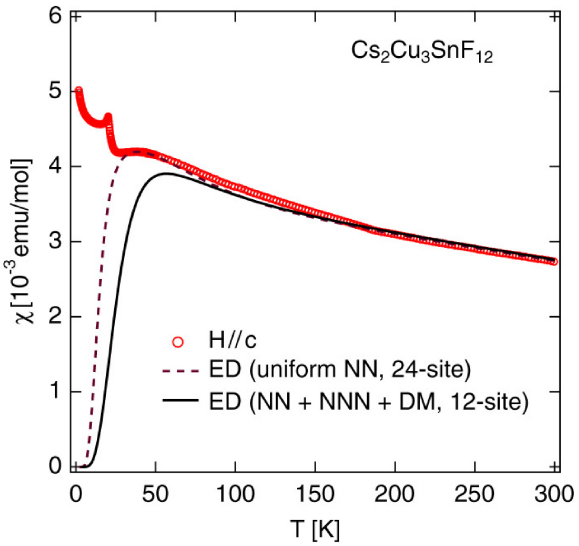

Fig. 26. (Color online) Temperature dependence of magnetic susceptibility in $Cs_2Cu_3SnF_{12}$. The dashed line denotes the result obtained by exact diagonalization for a 24-site uniform kagome cluster with $J = 20.7$ meV and $g = 2.49$, whereas the solid line denotes the result obtained for a 12-site distorted kagome cluster with $J^{mag}_{avg} = 19.8$ meV and the same interaction coefficients as those obtained from the analysis of spin-wave dispersions with $d_p = 0$ and $g = 2.43$. This figure is taken from Ref. 109. © (2014) The Physical Society of Japan.

three Heisenberg quantum spins 1/2 form a quartet and two degenerate low-energy doublets, and DMI lifts the degeneracy and selects the doublet with the (vector)-chirality opposite to **D**. As $D/J = 0.08$ is estimated for $ZnCu_3(OH)_6Cl_3$ from $D = 15$ K obtained by ESR measurements,[95] Cépas et al. suggested that this is compatible with the absence of a static moment (QSL-like)[94] in $ZnCu_3(OH)_6Cl_3$. However, as it is known that about 15% of Zn^{2+} ions separating the kagome planes in $ZnCu_3(OH)_6Cl_3$ have site exchanges with Cu^{2+} ions,[96] they will give random-bond exchange interactions in the kagome plane. Therefore, we would like to suggest an other possibility about the ground state of $ZnCu_3(OH)_6Cl_3$ suggested by Shimokawa et al.[97] From the ED method up to N = 30, Shimokawa et al. suggested that the QSL state observed in herbertsmithite might indeed be the randomness-induced QSL state, i.e., the random-singlet state.

Therefore, we need better ideal model substances for $S = 1/2$ kagome lattice antiferromagnets. Volborthite $Cu_3V_2O_7(OH)_22H_2O$[98] and vesignieite $BaCu_3V_2O_8(OH)_2$[99] were proposed as model substances by the Hiroi group at ISSP. However, a recent theory suggests the coupled trimer model for volborthite,[100] which can interpret a wide 1/3 plateau observed in the magnetization measurement of a single crystal up to 182 T using the Faraday rotation[101] and the spin nematic phase just above 26.3 T suggested by thermal measurements in high pulsed magnetic fields up to 33 T.[102] Furthermore, Furukawa and Momoi studied the effects of DMI in volborthite and showed that for a magnetic field perpendicular to the kagome layer, magnon excitations from the 1/3-plateau feel a Berry curvature due to the DMI, giving rise to a thermal Hall effect.[103] On the other hand, Okamoto et al.[99] suggested a gapless spin liquid for vesignieite from magnetic susceptibility and heat capacity measurements of a polycrystalline sample, which seemed consistent with the increases in g-value and linewidth below 20 K down to 1.9 K observed by high-field ESR.[104] However, as the quality of the polycrystalline sample increased, a long-range order was found at $T_N = 9$ K, and the importance of DMI in the system was discussed.[105,106] Therefore, the linewidths and line shifts observed by ESR were analyzed, and the DMI components were estimated.[107] Then, the dominance of in-plane DMI anisotropy was suggested, and it was proposed to strongly suppress quantum spin fluctuations and thus to promote long-range ordering rather than a spin-liquid state. This example also shows the importance of DMI in kagome lattice antiferromagnets.[107]

Ono et al. suggested Cs_2CuSnF_{12} as a new model substance of the $S = 1/2$ kagome lattice antiferromagnet.[108] The major advantage of Cs_2CuSnF_{12} is that they can obtain a large plate-like single crystal in the order of a few cm, which can be studied by inelastic neutron measurements and has no site exchange similar to herbertsmithite. The magnetic susceptibility measurement showed magnetic ordering at $T_N = 20$ K, which can be explained by DMI as discussed below.[108] Although the kagome plane is slightly distorted below $T_s = 185$ K owing to the structural phase transition, $J^{mag}_{avg} = 19.8$ meV (230 K) is estimated from the magnetic susceptibility result for H // c as shown in Fig. 26 using the theoretical result obtained by exact diagonalization for the 12-site kagome cluster.[109] The spin-wave dispersion, which was obtained by inelastic neutron scattering, was analyzed on the basis of the linear spin-wave theory using the spin Hamiltonian including the nearest-neighbor (NN) and next-nearest-neighbor (NNN) exchange interactions J_{ij} and J_2, respectively, and DMI (DM model).[109] The average spin-wave exchange interaction $J^{SW}_{avg} = (J_{11} + J_{12} + J_{13} + J_{14})/4 = 12.1$ meV and the out-of-plane DM factor $d_z = D^{//}_{ij}/J_{ij} = -0.29$ were obtained from the best fit (solid lines) shown in Fig. 27. The obtained $d_z = -0.29$ clearly shows that the origin of the magnetic ordering at $T_N = 20$ K for Cs_2CuSnF_{12} is DMI from Fig. 25. Furthermore, Ono et al. pointed out a large quantitative disagreement between $J^{SW}_{avg} = 12.1$ meV and $J^{mag}_{avg} = 19.8$ meV, where J^{mag}_{avg} is too large to interpret the spin-wave dispersion as shown in Fig. 27, and suggested the negative renormalization factor ($R = J^{SW}_{avg}/J^{mag}_{avg} = 0.61$) in Cs_2CuSnF_{12}.[109] On the other

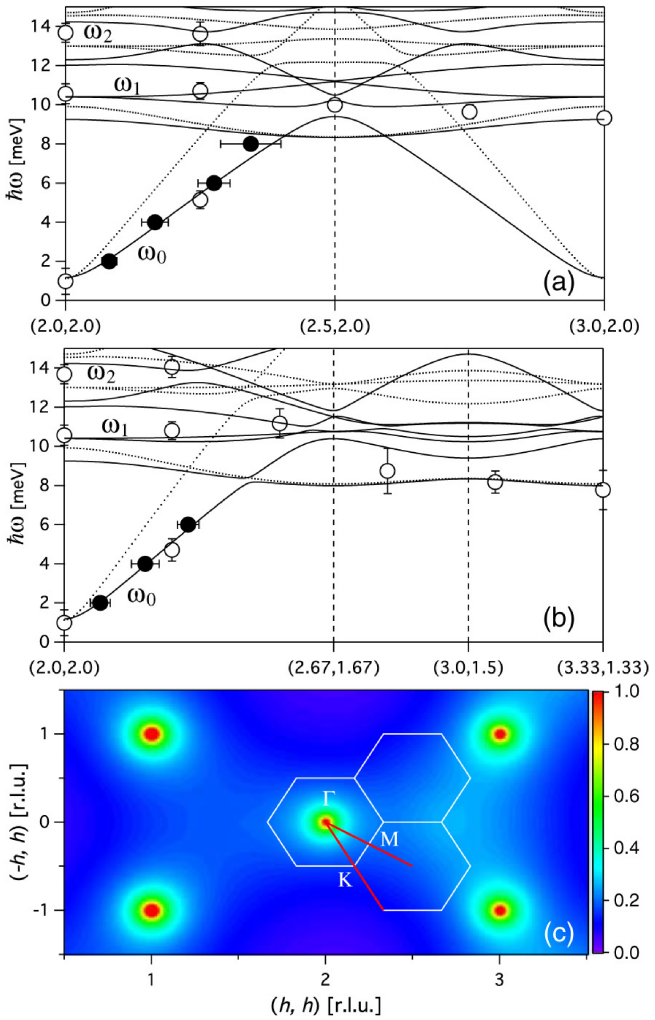

Fig. 27. (Color online) (a, b) Experimental data and calculated spin-wave dispersions along two high-symmetry directions denoted by thick red lines in (c). The open symbols indicate the data measured around $(2, 2, 0)$, whereas the closed symbols indicate the data measured at the equivalent point around $(0, 2, 0)$. The solid lines denote the best fit obtained using the DM model, and the dotted lines denote dispersions with $J_{\mathrm{avg}}^{\mathrm{mag}} = 19.8$ meV obtained from the magnetic susceptibility together with the remaining parameters equivalent to the best fit. (c) Calculated energy-integrated scattering intensity of $Cs_2Cu_2SnF_{12}$. This figure is taken from Ref. 109. © (2014) The Physical Society of Japan.

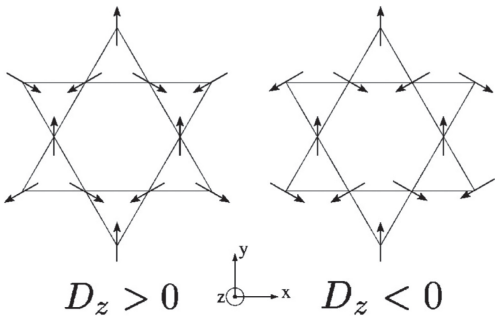

Fig. 28. $D \perp$ kagome plane. The spins lie in the kagome plane and the sign of D_z selects the chirality κ, where $\kappa = -1$ for $D_z > 0$ and $\kappa = +1$ for $D_z < 0$. Here, the convention for chirality is that the spins in the cross products appear to rotate anticlockwise around the hexagons. There is a global rotational degree of freedom around the z-axis. This figure is taken from Ref. 115. © (2002) American Physical Society.

hand, most $S = 1/2$ quantum spin antiferromagnets without frustration show the positive renormalization factor R reflecting the quantum effect. For instance, the $S = 1/2$ one-dimensional Heisenberg antiferromagnet shows $R = \pi/2 = 1.57$ (de Cloizeaux and Pearson mode),[110] which is confirmed by the neutron measurement of $CuCl_2 \cdot 2N(C_5D_5)$,[111] and $R = 1.21$ is reported for an $S = 1/2$ square-lattice antiferromagnet,[112] while $R = 0.90$ is estimated for the $S = 5/2$ kagome lattice antiferromagnet $KFe_3(OH)_6(SO_4)_2$ using the exchange constants determined from the dispersion relations[113] and magnetization and ESR measurements.[114] Here, R is expected to approach $R = 1$ as the spin quantum number S is increased to the classical limit. Therefore, the suggestion by Ono et al.,[109] in which the negative renormalization factor ($R = J_{\mathrm{avg}}^{\mathrm{SW}}/J_{\mathrm{avg}}^{\mathrm{mag}} = 0.61$) found in Cs_2CuSnF_{12} is the universal character of the kagome lattice antiferromagnet even it undergoes the magnetic order below $T_N = 20$ K by DMI, appears very interesting and requires further study in different model substances.

3.2 *Role of DMI in $S = 3/2$, $5/2$ kagome-lattice antiferromagnets: Determination of DMI by high-field ESR*

To understand the peculiar physical properties of $S = 1/2$ kagome-lattice antiferromagnets, fundamental studies on classical Heisenberg kagome-lattice antiferromagnets, where the 120° spin structure is stabilized at low temperature, together with the role of DMI are also required. Considering the model substances Fe ($S = 5/2$) and Cr ($S = 3/2$) jarosites in mind, Elhajal et al. studied low-temperature magnetic phases through mean-field approximation and classical Monté Carlo simulations considering mainly the nn exchange interactions and DMI ($\mathbf{D} \cdot (\mathbf{S}_i \times \mathbf{S}_j)$).[115] In the case where $\mathbf{D}$ is perpendicular to the kagome plane, the system undergoes a phase transition to a long-range ordered state. As all spins lie in the kagome plane, DMI acts similarly to an easy-plane anisotropy. Since it is a $\mathbf{q} = 0$ structure, all triangles have the same magnetic structure. Depending on the sign of D_z, two chiralities are found as shown in Fig. 28. However, in the case of $\mathbf{D}$ in the kagome plane, all spins have the same out-of-plane z component, giving rise to weak ferromagnetism perpendicular to the kagome plane. In this case, there is no longer a global rotational degree of freedom, and DMI acts more similarly to an easy-axis anisotropy. Now, a competition between exchange and DMI exists, and it induces the angle between the spins and the kagome plane, which depends on D/J. In the general case where $\mathbf{D}$ lies in the plane perpendicular to the exchange bond, which is the mirror plane between two sites according to Moriya's rule, the ground state depends on D_p/J and D_z/J as summarized in Fig. 29. Therefore, the determinations of D_p and D_z will be important for the experiments on the model substances.

Antiferromagnetic resonance (AFMR) measurement using multifrequency high-field ESR is a powerful means of determining magnetic anisotropies including DMI precisely. Therefore, Fujita et al. performed AFMR and magnetization measurements at 1.3 and 4.2 K, which is below $T_N = 65$ K, using pulsed magnetic fields up to 50 T on a $KFe_3(OH)_6(SO_4)_2$ (Fe-jarosite) single crystal, which is considered as the model substance of the $S = 5/2$ kagome-

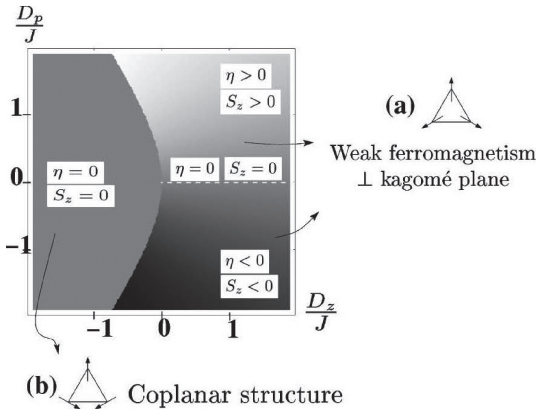

Fig. 29. Ground states obtained for different values of J (isotropic exchange), D_p, and D_z (in-plane and out-of-plane components of **D**, respectively). η is the angle between the spins and the kagome plane. This figure is taken from Ref. 115. © (2002) American Physical Society.

lattice antiferromagnet.[114] As the Weiss temperature $\Theta = -800$ K is obtained by magnetic susceptibility measurement, the frustration parameter $f = |\Theta|/T_N$ is about 12, indicating that this compound is highly frustrated. AFMR and magnetization results were analyzed using the DM model considering the exchange interactions, DMI, and Zeeman term. Six sublattices were considered below the magnetic transition $H_c = 16.4$ T owing to the weak antiferromagnetic interlayer coupling, while three sublattices were considered above H_c. The calculation can interpret the experimental results very well as shown in Fig. 30 with parameters $J = 42.3$ K, $D_p = 1.62$ K, and $D_z = 1.97$ K.[114] These parameters clearly suggest the spin structure (a) in Fig. 29, which is consistent with the powder neutron result suggesting the $\mathbf{q} = 0$ structure.[116] Here, note that the definition of chirality is different between Refs. 116 and 115 as clockwise or anticlockwise, while the conclusions are the same. The parameters $D_p = 2.29$ K and $D_z = 2.27$ K, which are rather consistent with those of Fujita et al.,[114] were also obtained by single crystal neutron scattering measurement,[113] but the results obtained by Fijita et al. have some advantages considering the error bars of the measurements. As $D_p = 1.62$ K and $D_z = 1.97$ K obtained from AFMR give $|D| = 2.55$ K, Fujita et al.[114] discussed the order of magnitude from $|D| = (\Delta g/g)J$.[2] As $g_a = 2.01$ and $g_c = 2.00$ are obtained by ESR measurements at room temperature, which are reasonable for Fe^{3+} ions with the orbital momentum L = 0, the estimated value $|D| = (\Delta g/g)J = 0.275$ K is obtained. This estimated value is one order of magnitude smaller than $|D| = 2.55$ K, which seems to be the remaining issue.

Cr-jarosite is an almost ideal compound for the model substance of the kagome-lattice antiferromagnet because it shows no ion exchange or lattice distortion, which are often seen in Cu-based or other Cr-based kagome lattice model substances. However, the previously reported magnetic properties of Cr-jarosite have been rather controversial, reflecting the difficulty in preparing high-quality samples, where a significant deficiency of Cr atoms, that is, 76%[117] or 95%[118] Cr occupancy, was suggested by neutron studies. On the other hand, no evidence of defects in Cr sites was obtained by an X-ray diffraction study for a Cr-jarosite

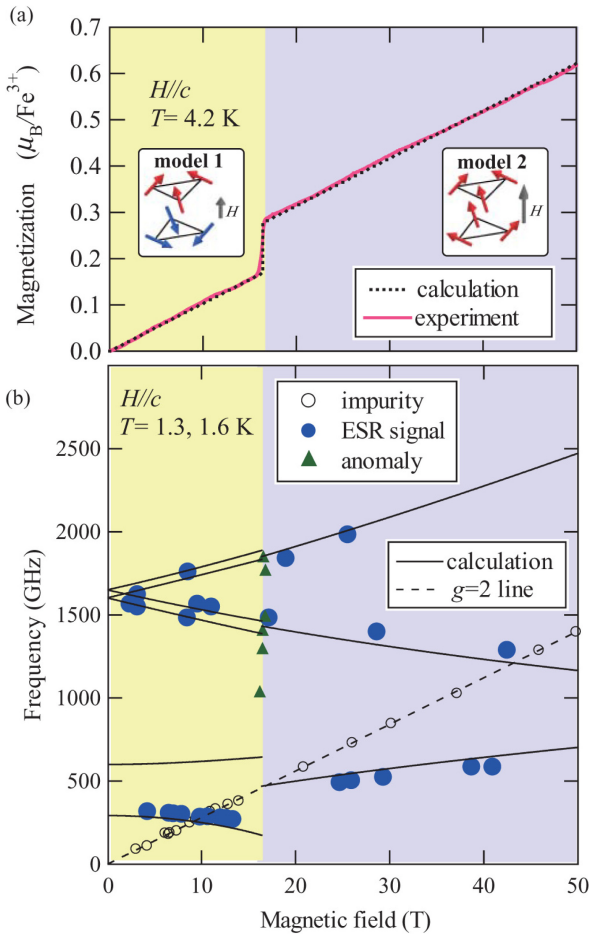

Fig. 30. (Color online) Comparison of magnetization curve and ESR modes of Fe-jarosite [$KFe_3(OH)_6(SO_4)_2$] between experiment and calculation for DM model. (a) Solid and broken lines represent the experimental (4.2 K) and calculated (0 K) magnetization curves, respectively. (b) Frequency-field plot of resonance fields taken at 1.3 K in pulsed fields and at 1.6 K in static fields for $H \parallel c$. The closed and open circles and triangles denote the resonance fields of intrinsic signals, and those of an impurity signal and an anomaly accompanied by the magnetic transition, respectively. This figure is taken from Ref. 114. © (2012) American Physical Society.

[$KCr_3(OH)_6(SO_4)_2$] single crystal synthesized by Okuta et al.[119] Using this high quality single crystal, Okuta et al. estimated the NN exchange interaction J as 6.15 K from the analysis of the magnetic susceptibility and revealed the spontaneous magnetization of $0.05\,\mu_B$/Cr along the c-axis (perpendicular to the kagome plane) below $T_N = 4.5$ K.[119] The obtained frustration parameter $f = |\Theta|/T_N$ is about 14, indicating that this compound is highly frustrated. To understand the role of DMI in this system, high-frequency high-field ESR measurements were performed using high-quality single crystals.[120] As rather sharp ESR absorption lines were obtained at 265 K, very precise g-values, $g_c = 1.9704 \pm 0.0002$ and $g_\xi = 1.9720 \pm 0.0003$, were obtained. Figure 31 shows the AFMR results obtained at 1.9 K.[120] A similar AFMR theory by Fujita et al.[114] was used with three sublattices because interlayer coupling seems to be negligible for Cr-jarosite. The parameters obtained by AFMR analysis are $J = 6.15$ K, $D_p = 0.27$ K, and $D_z = 0.07$ K.[120] The D estimated with Moriya's relation[2] using the obtained g-values is about 0.09 K, which is comparable to the obtained parameters. Moreover, the expected spontaneous magnetiza-

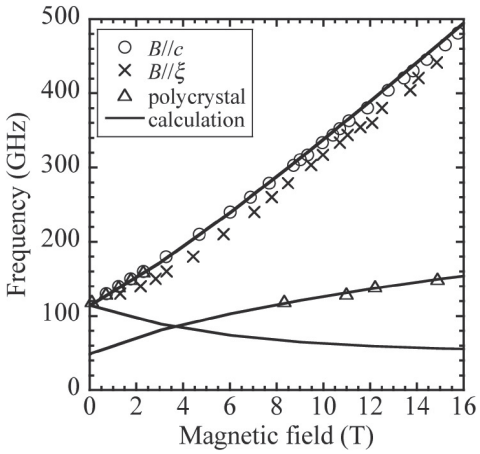

Fig. 31. Frequency-field diagram of AFMR observed for Cr-jarosite $[KCr_3(OH)_6(SO_4)_2]$ at 1.9 K. The open circles, crosses, and open triangles correspond to B // c, B // ξ, and polycrystal, respectively, where the c-axis is perpendicular to the kagome plane and the ξ-axis, which is in the kagome plane, is defined as the direction parallel to the edge of the triangle plane of the sample shape. The solid lines show the AFMR theory considering the DM interaction for B // c. This figure is taken from Ref. 120. © (2017) The Physical Society of Japan.

tion along the c-axis from these parameters is $0.074\,\mu_B$/Cr, which is comparable to that of $0.05\,\mu_B$/Cr obtained by Okuta et al.[119] Then, the obtained parameters, $D_z/J = 0.011$ and $D_p/J = 0.044$, give the ground state (a) in Fig. 29, which is consistent with the observed weak ferromagnetism perpendicular to the kagome plane. This is also consistent with the magnetic structure in the plane suggested by the neutron result.[118] Furthermore, the angular dependence of the ESR linewidth from B // c to B // observed by X-band ESR shows the two-dimensional character.[120] In summary, all experimental results using the high-quality Cr-jarosite single crystal suggest that it is a good $S = 3/2$ kagome antiferromagnet model substance. Therefore, the comparison of dispersion relations between the $S = 1/2$ and $3/2$ kagome antiferromagnet model substances by neutron inelastic measurements will be a very interesting issue.

3.3 Determination of DMI in $S = 3/2$ honeycomb lattice antiferromagnet $Bi_3Mn_4O_{12}(NO_3)$ by high-field ESR

Theoretically, the honeycomb lattice antiferromagnet with the NN exchange interaction (J_1) is considered as a bipartite lattice similar to the square lattice, and the Néel ordered state is expected as the ground state. However, the spin frustration effect will prohibit the magnetic order in the honeycomb lattice if the NNN antiferromagnetic exchange interaction (J_2) is considered.[121,122] The ground state is disordered when α ($= J_2/J_1$) $> 1/6$ and ~ 0.15 for classical spins and $S = 3/2$, respectively.[121,122] On the other hand, experimental investigations were rare owing to the lack of a model substance. Therefore, $Bi_3Mn_4O_{12}(NO_3)$, the model substance of the $S = 3/2$ honeycomb lattice antiferromagnet, attracted considerable attention when Smirnova et al.[123] synthesized its powder sample by the hydrothermal method. Moreover, it showed no long-range order down to 0.4 K despite the large $|\theta| = 257$ K (Curie–Weiss temperature $\theta = -257$ K), indicating strong antiferromagnetic interactions. The spin liquid state was expected in $Bi_3Mn_4O_{12}(NO_3)$, and it attracted considerable attention.

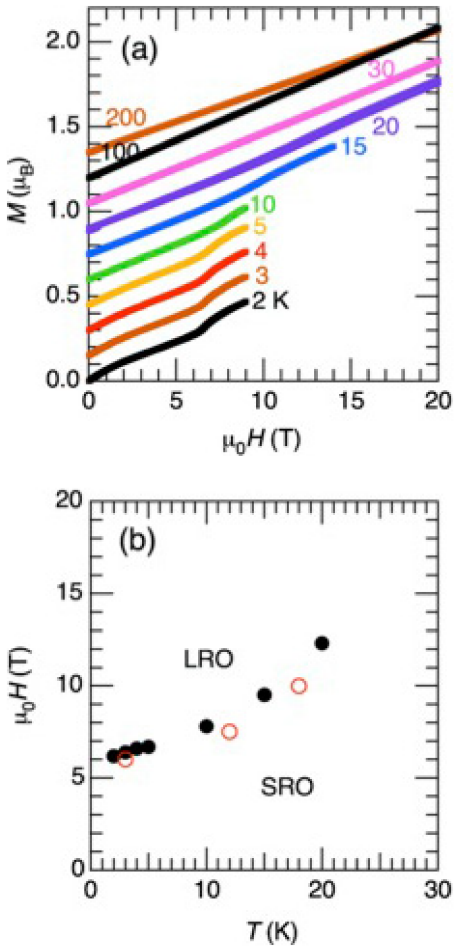

Fig. 32. (Color online) (a) Magnetization versus magnetic field in dc ($T \leq 10$ K) and pulsed field ($T \geq 15$ K) for $Bi_3Mn_4O_{12}(NO_3)$ in a temperature range between 2 and 200 K. (b) Temperature-magnetic field phase diagram. The filled and open circles show the data points determined from the magnetization and neutron scattering measurements, respectively. LRO and SRO stand for the long-range and short-range ordered phases, respectively. This figure is taken from Ref. 124. © (2010) American Physical Society.

Then, Matsuda et al.[124] found a small jump of $\sim 0.1\mu_B$/f.u. around 6–13 T below 20 K in the magnetization as shown in Fig. 32(a). To understand this metamagnetic transition, they also performed the neutron diffraction measurement under a magnetic field. With the application of a magnetic field at $T = 3$ K, the broad magnetic intensity at $H = 0$ T, which suggests the short-range antiferromagnetic order (SRO), is reduced, and the resolution-limited sharp magnetic Bragg peaks appear above $H \sim 6$ T, which suggests the long-range order (LRO) in the magnetic field.[124] The temperature-magnetic field phase diagram was determined as shown in Fig. 32(b) from the magnetization and neutron scattering measurements.[124] As the magnetic-field-induced phase transition, in which the short-range order expands into the long-range Néel order by applying the magnetic field, Matsuda et al. suggested that $Bi_3Mn_4O_{12}(NO_3)$ is located near the boundary of the order and disorder phases with α close to 0.15. The magnetic structure at LRO is determined as shown in Fig. 33 from the neutron diffraction measurement.[124] The size of the magnetic moment is about 2/3 of the full moment $3\mu_B$ for the Mn^{4+} ion. Matsuda et al. also suggested that the field-induced transition depends on the

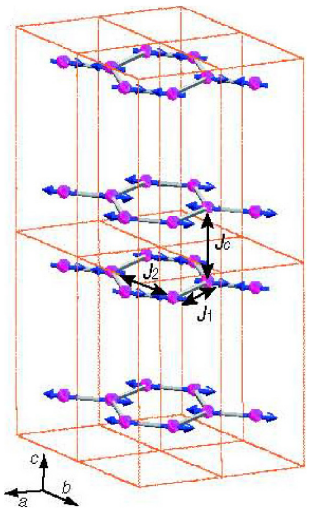

Fig. 33. (Color online) Magnetic structure of $Bi_3Mn_4O_{12}(NO_3)$ in magnetic field-induced phase. Mn^{4+} ions in $2 \times 2 \times 2$ unit cells are shown. The magnetic moments lie in the *ab*-plane, although the direction of the magnetic moments in the plane cannot be determined uniquely. The magnetic interactions J_1, J_2, and J_c are also shown. This figure is taken from Ref. 124. © (2010) American Physical Society.

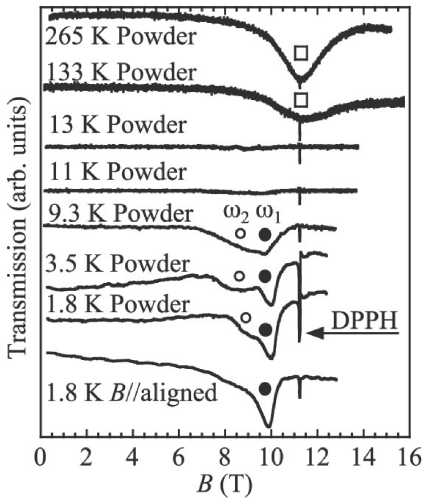

Fig. 34. Typical ESR spectra of $Bi_3Mn_4O_{12}(NO_3)$ observed at 315 GHz. The magnetic field is applied along the aligned direction in the case of the magnetically aligned sample. The sharp absorption lines observed around 11.2 T are diphenylpicrylhydrazyl (DPPH), which is the standard of $g = 2$. The solid and open circles correspond to the ω_1 and ω_2 modes, respectively. This figure is taken from Ref. 125. © (2012) American Physical Society.

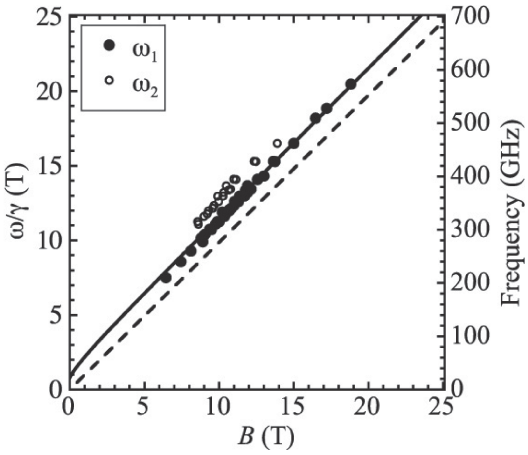

Fig. 35. Frequency-field diagram of $Bi_3Mn_4O_{12}(NO_3)$ obtained at 1.8 K. The solid and open circles correspond to the ω_1 and ω_2 modes, respectively, shown in Fig. 34. The solid line shows the AFMR mode [Eq. (14)] with $H_{DM} = 2.9$ T and $2H_E H'_A = 0.59$ T^2. This figure is taken from Ref. 125. © (2012) American Physical Society.

magnetic field direction because a broad signal around 1.6 Å^{-1} at 10 T, which is the remnant of the broad peak observed at $H = 0$ T in the neutron diffraction measurement, exists.[124] Therefore, they suggested that DMI may be an origin of anisotropy in an isotropic Heisenberg system, since the crystal structure (P3) does not have the inversion symmetry, and an origin of the ferromagnetic component of $\sim 0.1\mu_B$/f.u. found in the metamagnetic phase of the magnetization. However, the small canted component due to DMI cannot be detected in their neutron diffraction measurements because it is a powder sample.[124] Finally, Matsuda et al. roughly estimated the exchange interactions from the relatively sharp magnetic excitation, whose maximum extended up to 9 meV, as observed by inelastic neutron measurement at $T = 5.5$ K and $H = 0$ T.[124] Assuming $J_2/J_1 = 0.15$ corresponding to the critical value and $J_c = 0.5J_1$, they obtained $J_1 = 2J_c = 1.4$ meV (16.2 K) and $J_2 = 0.20$ meV (2.3 K), which were in reasonably good agreement with the Curie–Weiss temperature of −257 K.[124]

To clarify DMI in $Bi_3Mn_4O_{12}(NO_3)$, high-field THz ESR was performed using the high-quality sample.[125] The quality of this sample was higher than that of the previous one[123] as confirmed by the disappearance of MnO_2 peaks in X-ray diffraction and specific heat measurements and the suppression of the increase in magnetic susceptibility at low temperatures.[125] Furthermore, to obtain information about the anisotropy, the magnetically aligned sample is prepared by mixing the powder sample and epoxy resin at a static magnetic field of 9 T at room temperature.[125] After 24 h, the epoxy resin hardens and the magnetically aligned sample is produced. The aligned direction is confirmed to be perpendicular to the *c*-axis by X-ray measurement. The typical ESR spectrum observed at 315 GHz is shown in Fig. 34.[125] A comparison of the powder and magnetically aligned samples in Fig. 34, clearly shows that the ω_1 mode comes from the H perpendicular *c*-axis (H // aligned direction) component, whereas the ω_2 mode comes from the H // c component. The frequency-field diagram obtained at 1.8 K is shown in Fig. 35.[125] As the ω_1 mode at 1.8 K appears above 6 T, which is in the LRO phase of Fig. 32(b), and is shifted to the lower field side and parallel to the paramagnetic resonance line ($g = 1.974$, the dashed line in Fig. 35) in the wide-magnetic-field region of 6–19 T, the ω_1 mode can be considered as the AFMR mode when H is perpendicular to the *c*-axis. Furthermore, this peculiar frequency-field relation resembles the AFMR mode obtained by Pincus,[126] assuming an easy-plane-type anisotropy and DMI with two sublattices. Here, the assumption of an easy-plane-type anisotropy seems to be consistent with the magnetic structure (Fig. 33) in the LRO phase. Therefore, the obtained results are analyzed by the AFMR mode equation[126]

$$(\omega/\gamma)^2 = H(H + H_{DM}) + 2H_E H'_A, \tag{14}$$

where ω, γ, H, H_{DM}, H_E, and H'_A correspond to angular frequency, gyromagnetic ratio, external field along the x-axis, DM field, exchange field, and small anisotropy field in the easy plane, respectively. Here, the xy-plane, y-axis, and z-axis correspond to the easy plane, easy axis, and direction of the D vector of DMI, respectively. In the case of $Bi_3Mn_4O_{12}(NO_3)$, the z-axis corresponds to the c-axis, which is consistent with the detailed symmetry discussion in Ref. 125. The AFMR mode (14) can interpret the observed mode ω_1 very well with $H_{DM} = 2.9\,T$ and $2H_E H'_A = 0.59\,T^2$ as shown in Fig. 35. By using $H_{DM} = DM$, $D = 1.3\,K$ is obtained by assuming the full sublattice moment M with $S = 3/2$. $D = 1.3\,K$ is comparable to the rough estimation of 0.3 K using Eq. (2) and the estimated exchange interaction $J_1 = 30.7\,K$[127] obtained by a quantum Monte Carlo simulation by Onishi et al.[127] Then, the cant angle θ is estimated to be 2.42° using the relation $\tan\theta = D/J_1$, which can be obtained on the basis of the molecular field theory. This $\theta = 2.42°$ gives the $0.28\mu_B$/f.u. ferromagnetic component assuming a $1.8\mu_B$[124] ordered moment suggested by the neutron experiment. The $0.28\mu_B$/f.u. ferromagnetic component can be used to interpret the observed magnetization jump of $0.1\mu_B$/f.u.[124] at the metamagnetic transition considering that the magnetization measurement was carried out with the powder sample. Finally, some discussions on the ground state of $Bi_3Mn_4O_{12}(NO_3)$ at low temperatures and magnetic fields will be presented.[125] No paramagnetic ESR was observed at 1.9 K below 160 GHz, which is unusual for the system with finite magnetic susceptibility or the finite magnetization at low temperatures. The temperature dependences of ESR at 80 and 160 GHz show the broadening of the linewidth as the temperature decreases, which are similar to the broadening observed at 315 GHz in the temperature range of 11–265 K as shown in Fig. 34. The broadening of the ESR line below 160 GHz,[125] which suggests the existence of a very strong spin fluctuation even at 1.9 K, is consistent with the very small correlation length suggested by the neutron experiment.[124] However, it is unclear at the moment if this very strong spin fluctuation at low temperatures is a sign of the spin-liquid state because we do not have good experimental guidelines to distinguish the spin-liquid state. Moreover, there are also a few suggestions[127,128] that J_2/J_1 in $Bi_3Mn_4O_{12}(NO_3)$ might be less than 0.15, which is inconsistent with the observed disordered phase at $H = 0\,T$ and the field-induced LRO above 6 T. Therefore, the theory including the DMI might be important to discuss the ground state of $Bi_3Mn_4O_{12}(NO_3)$.

4. Summary

DMI plays an important role in the magnetic properties of quantum spin systems and in the ESR in them. The OA theory of the $S = 1/2$ 1D antiferromagnet with the staggered field, which is partly governed by DMI, suggests rich physics observed by ESR, such as the breather modes in the breather regime, the peculiar $(H/T)^n$ dependences of the linewidth ($n = 2$) and resonance shift ($n = 3$) in the spinon regime, and the T-dependence of the linewidth above the spinon regime. As they are confirmed experimentally by ESR in many model substances, such as Cu benzoate or $KCuGaF_6$, the OA theory is rather established. Furthermore, the theory suggesting the splitting of ESR in the $S = 1/2$ 1D antiferromagnet with the uniform DMI was confirmed in Cs_2CuCl_4, $K_2CuSO_4Br_2$, and $Na_2CuSO_4Cl_2$. Next, possible mechanisms for the singlet–triplet ESR transitions, which are typically forbidden for the magnetic dipole transition but observed in many quantum spin systems, are introduced. The magnetic dipole transition due to the mixing of the singlet and triplet states by DMI or staggered magnetic fields and the electric dipole transition coming from a dynamical DMI induced by the ac electric field are examined with several experimental examples. The selection rules based on the magnetic dipole transition due to the mixing of the singlet and triplet states by DMI are also discussed, while the consideration of the staggered field coming from the staggered g-tensor is also required in many real systems. Then, the determination of the ground state in the strongly frustrated $S = 1/2$ or $3/2$ kagome-lattice antiferromagnets by DMI, which exists in the kagome-lattice from the crystal symmetry, is considered in connection with the theoretical and experimental results of several model substances. Finally, the role and determination of DMI by ESR in the honeycomb lattice antiferromagnet $Bi_3Mn_4O_{12}(NO_3)$ are discussed.

Acknowledgment The author would like to thank Dr. Shunsuke C. Furuya (Univ. of Tokyo), Professor S. Kimura (IMR. Tohoku Univ.), Professor H. Tanaka (Tokyo Inst. Tech.), Professor T. Sakai (Univ. of Hyogo), Professor D. Yamamoto (Nihon Univ.), Dr. M. Fujisawa (Tokyo Inst. Tech.), Professor Y. Matsuda (ISSP, Univ. of Tokyo), Professor M. Hagiwara (Osaka Univ.), Professor H. Nojiri and Dr. M. Akaki (IMR. Tohoku Univ.), Dr. T. Shimokawa (OIST), and Professor H. Kawamura (Osaka Univ., Kobe Univ.) for stimulating discussions.

*hohta@kobe-u.ac.jp

1) I. Dzyaloshinsky, J. Phys. Chem. Solids **4**, 241 (1958).
2) T. Moriya, Phys. Rev. **120**, 91 (1960).
3) S. Blundell, *Magnetism in Condensed Matter* (Oxford University Press, Oxford, U.K., 2001) Oxford Master Series in Condensed Matter Physics, p. 81.
4) M. Oshikawa and I. Affleck, Phys. Rev. Lett. **82**, 5136 (1999).
5) M. Oshikawa and I. Affleck, Phys. Rev. B **65**, 134410 (2002).
6) M. Oshikawa, J. Phys. Soc. Jpn. **72** [Suppl. B], 36 (2003).
7) K. Okuda, H. Hata, and M. Date, J. Phys. Soc. Jpn. **33**, 1574 (1972).
8) K. Yu. Povarov, A. I. Smirnov, O. A. Starykh, S. V. Petrov, and A. Ya. Shapiro, Phys. Rev. Lett. **107**, 037204 (2011).
9) Proceedings of the International Workshop on Application of Submillimeter Wave Electron Spin Resonance for Novel Magnetic Systems, J. Phys. Soc. Jpn. **72 Suppl B** (2003).
10) H. Ohta and T. Sakai, Appl. Magn. Reson. **52**, 263 (2021).
11) M. Oshikawa and I. Affleck, Phys. Rev. Lett. **79**, 2883 (1997).
12) K. Oshima, K. Okuda, and M. Date, J. Phys. Soc. Jpn. **44**, 757 (1978).
13) D. C. Dender, P. R. Hammer, D. H. Reich, C. Broholm, and G. Aeppli, Phys. Rev. Lett. **79**, 1750 (1997).
14) T. Asano, H. Nojiri, Y. Inagaki, J. P. Boucher, T. Sakon, Y. Ajiro, and M. Motokawa, Phys. Rev. Lett. **84**, 5880 (2000).
15) S. A. Zvyagin, A. K. Kolezhuk, J. Krzystek, and R. Feyerherm, Phys. Rev. Lett. **93**, 027201 (2004).
16) S. A. Zvyagin, A. K. Kolezhuk, J. Krzystek, and R. Feyerherm, Phys. Rev. Lett. **95**, 017207 (2005).
17) I. Umegaki, H. Tanaka, T. Ono, H. Uekusa, and H. Nojiri, Phys. Rev. B **79**, 184401 (2009).
18) H. Ohta, S. Okubo, K. Kawakami, D. Fukuoka, Y. Inagaki, T. Kunimoto, and Z. Hiroi, J. Phys. Soc. Jpn. **72** [Suppl. B], 26 (2003).
19) S. C. Furuya and M. Oshikawa, Phys. Rev. Lett. **109**, 247603 (2012).
20) J. Z. Zhao, X. Q. Wang, T. Xiang, Z. B. Su, and L. Yu, Phys. Rev. Lett. **90**, 207204 (2003).
21) H. Nojiri, Y. Ajiro, T. Asano, and J.-P. Boucher, New J. Phys. **8**, 218 (2006).
22) F. H. L. Essler, A. Furusaki, and T. Hikihara, Phys. Rev. B **68**, 064410 (2003).

23) I. Affleck and M. Oshikawa, Phys. Rev. B **60**, 1038 (1999).
24) S. A. Zvyagin, E. Čižmár, M. Ozerov, J. Wosnitza, R. Feyerherm, S. R. Manmana, and F. Mila, Phys. Rev. B **83**, 060409(R) (2011).
25) Y. Ajiro, S. Matsukawa, T. Yamada, and T. Haseda, J. Phys. Soc. Jpn. **39**, 259 (1975).
26) H. Ohta, S. Imagawa, H. Ushiroyama, M. Motokawa, O. Fujita, and J. Akimitsu, J. Phys. Soc. Jpn. **63**, 2870 (1994).
27) S. V. Demishev, A. V. Semeno, N. E. Sluchanko, N. A. Samarin, A. N. Vasil'ev, and L. I. Leonyuk, Sov. Phys. JETP **85**, 943 (1997).
28) I. Yamada, H. Fujii, and M. Hidaka, J. Phys.: Condens. Matter **1**, 3397 (1989).
29) I. Yamada, M. Nishi, and J. Akimitsu, J. Phys.: Condens. Matter **8**, 2625 (1996).
30) I. Yamada, H. Manaka, H. Sawa, M. Nishi, M. Isobe, and Y. Ueda, J. Phys. Soc. Jpn. **67**, 4269 (1998).
31) R. Coldea, D. A. Tennant, A. M. Tsvelik, and Z. Tylczynski, Phys. Rev. Lett. **86**, 1335 (2001).
32) D. Yamamoto, T. Sakurai, R. Okuto, S. Okubo, H. Ohta, H. Tanaka, and Y. Uwatoko, Nat. Commun. **12**, 4263 (2021).
33) A. I. Smirnov, T. A. Soldatov, K. Yu. Povarov, M. Hälg, W. E. A. Lorenz, and A. Zheludev, Phys. Rev. B **92**, 134417 (2015).
34) K. Y. Povarov, T. A. Soldatov, R.-B. Wang, A. Zheludev, A. I. Smirnov, and O. A. Starykh, Phys. Rev. Lett. **128**, 187202 (2022).
35) A. Keselman, L. Balents, and O. A. Starykh, Phys. Rev. Lett. **125**, 187201 (2020).
36) M. Fujihala, Y. Sakuma, S. Mitsuda, A. Nakao, K. Munakata, R. A. Mole, S. Yano, D. H. Yu, K. Takehana, Y. Imanaka, M. Akaki, S. Okubo, and H. Ohta, Phys. Rev. B **105**, 144410 (2022).
37) S. A. Zvyagin, D. Kamenskyi, M. Ozerov, J. Wosnitza, M. Ikeda, T. Fujita, M. Hagiwara, A. I. Smirnov, T. A. Soldatov, A. Ya. Shapiro, J. Krzystek, R. Hu, H. Ryu, C. Petrovic, and M. E. Zhitomirsky, Phys. Rev. Lett. **112**, 077206 (2014).
38) O. A. Starykh, H. Katsura, and L. Balents, Phys. Rev. B **82**, 014421 (2010).
39) R. Coldea, D. A. Tennant, K. Habicht, P. Smeibidl, C. Wolters, and Z. Tylczynski, Phys. Rev. Lett. **88**, 137203 (2002).
40) S. A. Zvyagin, D. Graf, T. Sakurai, S. Kimura, H. Nojiri, J. Wosnitza, H. Ohta, T. Ono, and H. Tanaka, Nat. Commun. **10**, 1064 (2019).
41) T. Sakurai, S. Okubo, and H. Ohta, J. Magn. Reson. **280**, 3 (2017).
42) T. Sakurai, S. Kimura, M. Kimata, H. Nojiri, S. Awaji, S. Okubo, H. Ohta, Y. Uwatoko, K. Kudo, and Y. Koike, J. Magn. Reson. **296**, 1 (2018).
43) T. Nikuni, M. Oshikawa, A. Oosawa, and H. Tanaka, Phys. Rev. Lett. **84**, 5868 (2000).
44) W. Lu, J. Tuchendler, M. von Ortenberg, and J. P. Renard, Phys. Rev. Lett. **67**, 3716 (1991).
45) H. Nojiri, H. Ohta, S. Okubo, O. Fujita, J. Akimitsu, and M. Motokawa, J. Phys. Soc. Jpn. **68**, 3417 (1999).
46) H. Tanaka, K. Takatsu, W. Shiramura, T. Kambe, H. Nojiri, T. Yamada, S. Okubo, H. Ohta, and M. Motokawa, Physica B **246–247**, 545 (1998).
47) H. Ohta, S. Okubo, T. Kamikawa, T. Kunimoto, Y. Inagaki, H. Kikuchi, T. Saito, M. Azuma, and M. Takano, J. Phys. Soc. Jpn. **72**, 2464 (2003).
48) M. Fujisawa, K. Shiraki, S. Okubo, H. Ohta, M. Yoshida, H. Tanaka, and T. Sakai, Phys. Rev. B **80**, 012408 (2009).
49) H. Nojiri, H. Kageyama, Y. Ueda, and M. Motokawa, J. Phys. Soc. Jpn. **72**, 3243 (2003).
50) T. Sakai and H. Shiba, J. Phys. Soc. Jpn. **63**, 867 (1994).
51) T. Sakai, J. Phys. Soc. Jpn. **72** [Suppl. B], 53 (2003).
52) S. Kimura, M. Matsumoto, M. Akaki, M. Hagiwara, K. Kindo, and H. Tanaka, Phys. Rev. B **97**, 140406 (2018).
53) H. Katsura, N. Nagaosa, and A. V. Balatsky, Phys. Rev. Lett. **95**, 057205 (2005).
54) I. A. Sergienko and E. Dagotto, Phys. Rev. B **73**, 094434 (2006).
55) T. A. Kaplan and S. D. Mahanti, Phys. Rev. B **83**, 174432 (2011).
56) O. Cépas and T. Ziman, Phys. Rev. B **70**, 024404 (2004).
57) Z. Wang, D. Kamenskyi, O. Cepas, M. Schmidt, D. L. Quintero-Castro, A. T. M. N. Islam, B. Lake, A. A. Aczel, H. A. Dabkowska, A. B. Dabkowski, G. M. Luke, Y. Wan, A. Loidl, M. Ozerov, J. Wosnitza, S. A. Zvyagin, and J. Deisenhofer, Phys. Rev. B **89**, 174406 (2014).
58) F. D. M. Haldane, Phys. Lett. A **93**, 464 (1983); F. D. M. Haldane, Phys. Rev. Lett. **50**, 1153 (1983).
59) J. P. Renard, M. Verdaguer, L. P. Regnault, W. A. C. Erkelens, J. Rossat-Mignod, and W. G. Stirling, Europhys. Lett. **3**, 945 (1987).
60) K. Katsumata, H. Hori, T. Takeuchi, M. Date, A. Yamagishi, and J. P. Renard, Phys. Rev. Lett. **63**, 86 (1989).
61) M. Chiba, Y. Ajiro, H. Kikuchi, T. Kubo, and T. Morimoto, Phys. Rev. B **44**, 2838 (1991).
62) M. Hase, I. Terasaki, and K. Uchinokura, Phys. Rev. Lett. **70**, 3651 (1993).
63) S. Kokado and N. Suzuki, Proc. 4th Int. Symposium on Advanced Physical Fields, 1999, p. 243.
64) T. Sakai, O. Cépas, and T. Ziman, J. Phys. Soc. Jpn. **69**, 3521 (2000).
65) T. Sakai, Appl. Magn. Reson. **52**, 507 (2021).
66) H. Kageyama, K. Yoshimura, R. Stern, N. V. Mushnikov, K. Onizuka, M. Kato, K. Kosuge, C. P. Slichter, T. Goto, and Y. Ueda, Phys. Rev. Lett. **82**, 3168 (1999).
67) B. S. Shastry and B. Sutherland, Physica B **108**, 1069 (1981).
68) K. Onizuka, H. Kageyama, Y. Narumi, K. Kindo, Y. Ueda, and T. Goto, J. Phys. Soc. Jpn. **69**, 1016 (2000).
69) O. Cépas, K. Kakurai, L. P. Regnault, T. Ziman, J. P. Boucher, N. Aso, M. Nishi, H. Kageyama, and Y. Ueda, Phys. Rev. Lett. **87**, 167205 (2001).
70) K. Kakurai, N. Aso, K. Nukui, M. Nishi, H. Kageyama, Y. Ueda, H. Kadowaki, and O. Cépas, in *Quantum Properties of Low-Dimensional Antiferromagnets*, ed. Y. Ajiro and J. P. Boucher (Kyushu University Press, Fukuoka, 2002).
71) S. Miyahara and K. Ueda, J. Phys. Soc. Jpn. **69** [Suppl. B], 72 (2000).
72) Y. H. Matsuda, N. Abe, S. Takeyama, H. Kageyama, P. Corboz, A. Honecker, S. R. Manmana, G. R. Foltin, K. P. Schmidt, and F. Mila, Phys. Rev. Lett. **111**, 137204 (2013).
73) A. Koga and N. Kawakami, Phys. Rev. Lett. **84**, 4461 (2000).
74) H. Ohta, T. Sakurai, R. Matsui, K. Kawasaki, Y. Hirao, S. Okubo, K. Matsubayashi, Y. Uwatoko, K. Kudo, and Y. Koike, J. Phys. Chem. B **119**, 13755 (2015).
75) T. Sakurai, K. Fujimoto, R. Matsui, K. Kawasaki, S. Okubo, H. Ohta, K. Matsubayashi, Y. Uwatoko, and H. Tanaka, J. Magn. Reson. **259**, 108 (2015).
76) Y. Takushima, A. Koga, and N. Kawakami, J. Phys. Soc. Jpn. **70**, 1369 (2001).
77) T. Sakurai, Y. Hirao, K. Hijii, S. Okubo, H. Ohta, Y. Uwatoko, K. Kudo, and Y. Koike, J. Phys. Soc. Jpn. **87**, 033701 (2018).
78) T. Sakurai, K. Hijii, and H. Ohta, Butsuri **74**, 633 (2019) [in Japanese].
79) M. E. Zayed, Ch. Rüegg, J. Larrea, J. A. M. Läuchli, C. Panagopoulos, S. S. Saxena, M. Ellerby, D. F. McMorrow, Th. Strässle, S. Klotz, G. Hamel, R. A. Sadykov, V. Pomjakushin, M. Boehm, M. Jiménez-Ruiz, A. Schneidewind, E. Pomjakushina, M. Stingaciu, K. Conder, and H. M. Rønnow, Nat. Phys. **13**, 962 (2017).
80) G. Misguich and M. Oshikawa, J. Phys. Soc. Jpn. **73**, 3429 (2004).
81) S. Kimura, K. Kakihata, Y. Sawada, K. Watanabe, M. Matsumoto, M. Hagiwara, and H. Tanaka, Nat. Commun. **7**, 12822 (2016).
82) X.-G. Zhou, Y. Yao, Y. H. Matsuda, A. Ikeda, A. Matsuo, K. Kindo, and H. Tanaka, Phys. Rev. Lett. **125**, 267207 (2020).
83) H. Kikuchi, Y. Fujii, M. Chiba, S. Mitsudo, and T. Idehara, Physica B **329–333**, 967 (2003).
84) H. Kikuchi, Y. Fujii, M. Chiba, S. Mitsudo, T. Idehara, T. Tonegawa, K. Okamoto, T. Sakai, T. Kuwai, and H. Ohta, Phys. Rev. Lett. **94**, 227201 (2005).
85) K. Okamoto, T. Tonegawa, Y. Takahashi, and M. Kaburagi, J. Phys.: Condens. Matter **11**, 10485 (1999).
86) T. Tonegawa, K. Okamoto, T. Hikihara, Y. Takahashi, and M. Kaburagi, J. Phys. Soc. Jpn. **69** [Suppl. A], 332 (2000).
87) B. Gu and G. Su, Phys. Rev. Lett. **97**, 089701 (2006).
88) H. Jeschke, I. Opahle, H. Kandpal, R. Valentí, H. Das, T. Saha-Dasgupta, O. Janson, H. Rosner, A. Brühl, B. Wolf, M. Lang, J. Richter, S. Hu, X. Wang, R. Peters, T. Pruschke, and A. Honecker, Phys. Rev. Lett. **106**, 217201 (2011).
89) S. Okubo, A. Taketani, H. Ohta, T. Kunimoto, Y. Inagaki, T. Saito, M. Azuma, M. Takano, and H. Kikuchi, Prog. Theor. Phys. Suppl. **159**, 11 (2005).
90) M. Mekata, Phys. Today **56** [2], 12 (2003).
91) B. Levi, Phys. Today **60** [2], 16 (2007).
92) O. Cépas, C. M. Fong, P. W. Leung, and C. Lhuillie, Phys. Rev. B **78**, 140405(R) (2008).

93) M. P. Shores, E. A. Nytko, B. M. Bartlett, and D. G. Nocera, J. Am. Chem. Soc. **127**, 13462 (2005).
94) P. Mendels, F. Bert, M. A. de Vries, A. Olariu, A. Harrison, F. Duc, J. C. Trombe, J. S. Lord, A. Amato, and C. Baines, Phys. Rev. Lett. **98**, 077204 (2007).
95) A. Zorko, S. Nellutla, J. van Tol, L. C. Brunel, F. Bert, F. Duc, J. C. Trombe, M. A. de Vries, A. Harrison, and P. Mendels, Phys. Rev. Lett. **101**, 026405 (2008).
96) D. E. Freedman, T. H. Han, A. Prodi, P. Müller, Q.-Z. Huang, Y.-S. Chen, S. M. Webb, Y. S. Lee, T. M. McQueen, and D. G. Nocera, J. Am. Chem. Soc. **132**, 16185 (2010).
97) T. Shimokawa, K. Watanabe, and H. Kawamura, Phys. Rev. B **92**, 134407 (2015).
98) Z. Hiroi, M. Hanawa, N. Kobayashi, M. Nohara, H. Takagi, Y. Kato, and M. Takigawa, J. Phys. Soc. Jpn. **70**, 3377 (2001).
99) Y. Okamoto, H. Yoshida, and Z. Hiroi, J. Phys. Soc. Jpn. **78**, 033701 (2009).
100) O. Janson, S. Furukawa, T. Momoi, P. Sindzingre, J. Richter, and K. Held, Phys. Rev. Lett. **117**, 037206 (2016).
101) D. Nakamura, T. Yamashita, H. Ishikawa, Z. Hiroi, and S. Takeyama, Phys. Rev. B **98**, 020404(R) (2018).
102) Y. Kohama, H. Ishikawa, A. Matsuo, K. Kindo, N. Shannon, and Z. Hiroi, Proc. Natl. Acad. Sci. U.S.A. **116**, 10686 (2019).
103) S. Furukawa and T. Momoi, J. Phys. Soc. Jpn. **89**, 034711 (2020).
104) W.-M. Zhang, H. Ohta, S. Okubo, M. Fujisawa, T. Sakurai, Y. Okamoto, H. Yoshida, and Z. Hiroi, J. Phys. Soc. Jpn. **79**, 023708 (2010).
105) J. A. Quilliam, F. Bert, R. H. Colman, D. Boldrin, A. S. Wills, and P. Mendels, Phys. Rev. B **84**, 180401(R) (2011).
106) H. Yoshida, Y. Michiue, E. Takayama-Muromachi, and M. Isobe, J. Mater. Chem. **22**, 18793 (2012).
107) A. Zorko, F. Bert, A. Ozarowski, J. van Tol, D. Boldrin, A. S. Wills, and P. Mendels, Phys. Rev. B **88**, 144419 (2013).
108) T. Ono, K. Morita, M. Yano, H. Tanaka, K. Fujii, H. Uekusa, Y. Narumi, and K. Kindo, Phys. Rev. B **79**, 174407 (2009).
109) T. Ono, K. Matan, Y. Nambu, T. J. Sato, K. Katayama, S. Hirata, and H. Tanaka, J. Phys. Soc. Jpn. **83**, 043701 (2014).
110) J. des Cloizeaux and J. J. Pearson, Phys. Rev. **128**, 2131 (1962).
111) Y. Endoh, G. Shirane, R. Birgeneau, P. Richards, and S. Holt, Phys. Rev. Lett. **32**, 170 (1974).
112) H. M. Rønnow, D. F. McMorrow, R. Coldea, A. Harrison, I. D. Youngson, T. G. Perring, G. Aeppli, O. Syljuåsen, K. Lefmann, and C. Rischel, Phys. Rev. Lett. **87**, 037202 (2001).
113) K. Matan, D. Grohol, D. G. Nocera, T. Yildirim, A. B. Harris, S. H. Lee, S. E. Nagler, and Y. S. Lee, Phys. Rev. Lett. **96**, 247201 (2006).
114) T. Fujita, H. Yamaguchi, S. Kimura, T. Kashiwagi, M. Hagiwara, K. Matan, D. Grohol, D. G. Nocera, and Y. S. Lee, Phys. Rev. B **85**, 094409 (2012).
115) M. Elhajal, B. Canals, and C. Lacroix, Phys. Rev. B **66**, 014422 (2002).
116) T. Inami, M. Nishiyama, S. Maegawa, and Y. Oka, Phys. Rev. B **61**, 12181 (2000).
117) S.-H. Lee, C. Broholm, M. F. Collins, L. Heller, A. P. Ramirez, C. Kloc, E. Bucher, R. W. Erwin, and N. Lacevic, Phys. Rev. B **56**, 8091 (1997).
118) T. Inami, T. Morimoto, M. Nishiyama, S. Maegawa, Y. Oka, and H. Okumura, Phys. Rev. B **64**, 054421 (2001).
119) K. Okuta, S. Hara, H. Sato, Y. Narumi, and K. Kindo, J. Phys. Soc. Jpn. **80**, 063703 (2011).
120) S. Okubo, R. Nakata, S. Ikeda, N. Takahashi, T. Sakurai, W.-M. Zhang, H. Ohta, T. Shimokawa, T. Sakai, K. Okuta, S. Hara, and H. Sato, J. Phys. Soc. Jpn. **86**, 024703 (2017).
121) S. Katsura, T. Ide, and T. Morita, J. Stat. Phys. **42**, 381 (1986).
122) K. Takano, Phys. Rev. B **74**, 140402(R) (2006).
123) O. Smirnova, M. Azuma, N. Kumada, Y. Kusano, M. Matsuda, Y. Shimakawa, T. Takei, Y. Yonesaki, and N. Kinomura, J. Am. Chem. Soc. **131**, 8313 (2009).
124) M. Matsuda, M. Azuma, M. Tokunaga, Y. Shimakawa, and N. Kumada, Phys. Rev. Lett. **105**, 187201 (2010).
125) S. Okubo, T. Ueda, H. Ohta, W. Zhang, T. Sakurai, N. Onishi, M. Azuma, Y. Shimakawa, H. Nakano, and T. Sakai, Phys. Rev. B **86**, 140401(R) (2012).
126) P. Pincus, Phys. Rev. Lett. **5**, 13 (1960).
127) N. Onishi, K. Oka, M. Azuma, Y. Shimakawa, Y. Motome, T. Taniguchi, M. Hiraishi, M. Miyazaki, T. Masuda, A. Koda, K. M. Kojima, and R. Kadono, Phys. Rev. B **85**, 184412 (2012).
128) R. Ganesh, D. N. Sheng, Y. J. Kim, and A. Paramekanti, Phys. Rev. B **83**, 144414 (2011).

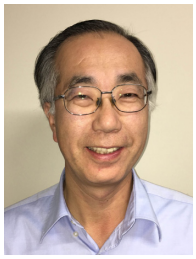

Hitoshi Ohta received his bachelor degree at University of Tokyo, master and doctor of science degrees at Tokyo University of Science. He joined Kobe University in 1987 and became a Professor at Molecular Photoscience Research Center, Kobe University since 2001. He has been developing multiextreme THz ESR system at Kobe University, and served as Presidents of International EPR (ESR) Society, Asia-Pacific EPR/ESR Society, and SEST.